Maximizing the detection of *thermal imprints* in civil engineering composites via numerical and thermographic results pre-processed by a groundbreaking mathematical approach

Stefano Sfarra [a*], Antonio Cicone [b,c,d], Bardia Yousefi [e], Stefano Perilli [f], Leonardo Robol [g], Xavier P.V. Maldague [e]

[a] Department of Industrial and Information Engineering and Economics (DIIIE), University of L'Aquila, Piazzale E. Pontieri 1, I-67100, L'Aquila, Italy

[b] Department of Information Engineering and Computer Science and Mathematics, University of L'Aquila, Via Vetoio 1, I-67100, L'Aquila, Italy

[c] Istituto di Astrofisica e Planetologia Spaziali, Istituto Nazionale di Astrofisica, Via del Fosso del Cavaliere, 100, I-00133, Roma, Italy

[d] Istituto Nazionale di Geofisica e Vulcanologia, Via di Vigna Murata 605, I-00143, Roma, Italy

[e] Department of Electrical and Computer Engineering, Laval University, 1065 avenue de la Médecine, G1V 0A6, Québec City (Quebec), Canada

[f] Independent Researcher, I-67100, Santa Rufina di Roio – L'Aquila, Italy

[g] Department of Mathematics, University of Pisa, L.go B. Pontecorvo 5, I-56127, Pisa, Italy

[*] Corresponding author's email: stefano.sfarra@univaq.it

Abstract

New composite materials are always subjected to non-destructive evaluation (NDE) prior to being placed on the market. This is to fully understand the *reactions* (i.e., development of defects) at the interface between two subsequent layers. Active infrared thermography (aIRT) can help in this regard, especially if anticipated by a simulation of the heat transfer from the exterior (lamp) to the interior (multilayer). Comsol Multiphysics® was used in this work as a tool by developing an innovative approach, which is designed –

on the one hand – to minimize the computational cost and – on the other hand – to optimize the radiation to be delivered. The innovation produced by our work also concerns the pre-processing step of the thermal images; in fact, the 2D Fast Iterative Filtering (FIF2) is here introduced, discussing its benefits in comparison to previously developed techniques. Pre-processed data were further analyzed during the post-processing step demonstrating the reliability of FIF2 in enhancing *thermal imprints*, which leads to an improved detection of subsurface features. In particular, enhanced thermal imprints highlight the shape of the grid of glass fibres present beneath an external coating of hemp fibres (and, in general, added to the whole specimen along the *x-y* vectors). This grid of glass fibres was recently introduced as an insulation material for buildings. A brief review of the use of the pre-processing step in aIRT allows the reader to better understand the decisive step forward provided by FIF2 combined with a clever numerical simulation in the applied thermal engineering field. Qualitative and quantitative IRT results are shown and discussed thoroughly. Finally, a validation among numerical and experimental (thermographic) data is provided thanks to the Parker (laser flash) method.

Keywords: infrared thermography; pre- and -post processing; computational fluid dynamics; thermal insulation; applied thermal engineering; heat transfer; 2D Fast Iterative Filtering.

1. Introduction

Pre-processing in thermal imagery is a step not so common as one might think. Post-processing is instead a routine step put in practice by authors to improve the “significance”, i.e., the reading of nuances, of thermal images. On the one hand, pre-processing is generally used to correct some parts of thermal images, affected by, e.g., dead pixels, vignetting, etc. On the other hand, pre-processing of thermal images is generally applied in medicine to detect cancers and distinguish false positives from false negatives.

As it is possible to see from the short review provided in the following (Diagram 1), the pre-processing step has rarely been used in heat transfer mechanisms when undetectable shapes to the naked eye (i.e., the so-called thermal imprints) need to be inversely retrieved.

Pre-processing of thermal images

From 1986 To 2021

From the earlier to the latest date

	Mechanical Engineering – Authors	Mechanical Engineering – Main idea	Environment – Authors	Environment – Main idea	Medicine – Authors	Medicine – Main idea	Imaging – Authors	Imaging – Main idea	Technical Physics – Authors	Technical Physics – Main idea
1	Hidalgo-Gato et al. [8]	Improvement of stabilization and matching phases in online welding monitoring processes.	Hidalgo-Gato et al. [12]	Detection and identification of contaminated soils by applying artificial neural networks (ANN).	Vardasca and Bajwa [4]	Evaluation of the best automatic edge detection algorithms and analysis via a homomorphic filter.	Seed et al. [1]	Comparison of visible and IR images.	Rainieri et al. [3]	Optimization of data processing via Wiener filter.
2	Murariu and Crasteti [11]	Image-enhancing, image pre-processing, histogram and flaw area evaluation of anticorrosive Al coatings.	Shanmugam and Chandira Sekaran [18]	The use of histogram equalization and segmentation of high-temperature zones via Fuzzy C Means (FCM) and modified ant lion optimization (MALO) stategies.			Creemer et al. [2]	Reconstruction of polarimetric images and application of receiver operating characteristic (ROC) curves.	Peng et al. [9]	Development of methods able to suppress the hot dome radiation and, therefore, able to reduce the image degradation.
3	Li et al. [13]	Quantitative evaluation of surface crack detection in metallic materials based on eddy current pulse thermography (ECPT) and a new segmentation algorithm.	Barreira et al. [23]	Data reduction, data processing and thermal indexes for the evaluation of humidification phenomenon in lightweight concrete specimens.			San Martin et al. [5]	Face recognition via nonuniformity correction (NUC) techniques.	Halloua et al. [13]	Modelling the relationship among thermal response and coating thickness using a laser pulse coupled with principal component analysis (PCA).
4	Kurpinski et al. [15]	The combined use of noise filtration, contrast enhancement operations, transformation of spatiotemporal structure of images, image segmentation, fusion of images and pattern recognition for identification and classification of defects in adhesively bonded joints.	Diaz et al. [25]	Detection of solar panels using unmanned aerial vehicles (UAVs) and computational techniques, one of which based on deep learning.			Liu et al. [6]	Target location based on image registration via four steps.	Moustakidis et al. [17]	Development and test of several excitations invariant techniques in addressing the unwanted effect of non-uniform heating in IR images also thanks to the use of modelling.

Diagram 1: … continue to next page ...

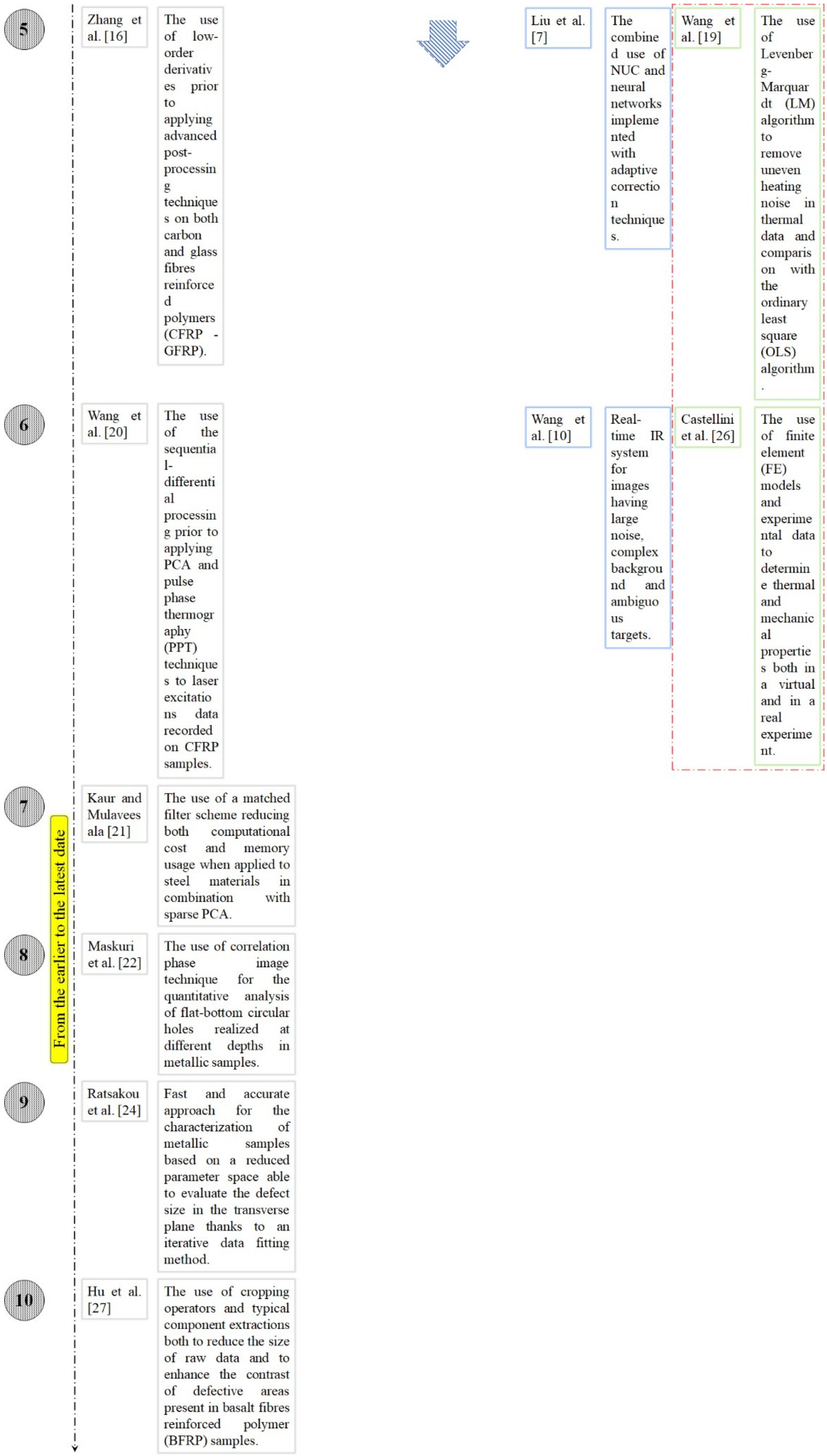

Diagram 1: Short review (from 1986 to 2021) of the works based on pre-processing algorithms for thermal images per field of application.

In total, twenty-seven manuscripts have been described in Diagram 1. Taking into account the 35-year time-frame, this number is certainly a representative sample.

It should be noticed that the present research falls into the renewable and clean-energy technologies theme that is strictly linked to the *technical physics* field mainly based on heat transfer concepts and thermodynamics. In fact, the authors studied an applied solution for improving energy efficiency and, therefore, for reducing emissions thanks to the use of natural fibres. As can be seen from Diag. 1, not much research has been conducted so far by considering the three cornerstones, (1) IRT – (2) pre- and post-processing – (3) *technical physics* (i.e., applied thermal engineering). Also, only in the papers [13], [17], and [26] the applied numerical modelling was used as a mean to proceed further with experimental analyses. Readers can refer to the column on the right side in Diag. 1, which is marked with a red dot-dashed rectangle. Therefore, it is worth looking into this line of research.

In this work the idea presented in [28] is further developed, by focusing the attention on a multilayer sample used in civil engineering as insulation. This multilayer sample has a coating of scattered hemp fibres, which has been recently developed and placed on the market [29-30]. The present work starts with a numerical modelling, which is used to study the behaviour of the heat flow inside the sample. This modelling, which is built step-by-step, is innovative since aimed at minimizing the computational cost without giving up on accuracy. Several tests were performed to choose the best heating time able to reach the deeper layer. The use of mathematical methods applied to raw thermal images explains how a useful and simple setup based on a thermal camera (working into the long-wave infrared spectrum) coupled with a PC and two lamps allows to obtain new and interesting results. Then, the innovative 2D Fast Iterative Filtering (FIF2), the generalization to 2D of the well-established Fast Iterative Filtering algorithm, e.g. [41] and [44], is presented in this work and compared with previously developed techniques. This technique is used in this work as a pre-processing algorithm, which allows to remove high frequency and low frequency oscillations from the thermal images. Pre-processed data were further analyzed in the post-processing step demonstrating the reliability of FIF2 to minimize the negative *impact* of thermal variations at the border of the sample, as well as the high-frequency oscillations due to noise, therefore, providing clear and precise *thermal imprints* to be segmented. The results (supported by a quantitative evaluation of the Precision, Recall, and Accuracy parameters) confirm the high ability of the proposed pre-processing FIF2 method. Computational performance like this cannot be found in any of the works published in the *technical physics* field in the last 35 years, which are summarized in the right most column of Diagram 1.

Also, the high insulation performance in term of thermal diffusivity of the coating layer made by scattered hemp fibres (i.e., an anisotropic material) was confirmed using the Parker method (i.e., the so-called laser flash method) [31], which has never been used, to the best of the authors knowledge, neither on this type of material nor applying the experimental setup here proposed. This is a direct validation of the numerical analyses performed in Comsol® environment, since it is centred on the material facing the heat source (i.e., the most important layer forming the multilayer specimen).

Therefore, the innovation brought to light from the current research with respect to Diag. 1 is based on three cornerstones:

- The conceptualization of the modelling phase;
- The output and performance provided by the innovative FIF2 pre-processing algorithm when applied on thermal images detecting *thermal imprints* (e.g., the so-called *thermal bridges* in civil engineering field);

The modality of application of the Parker's (laser flash) method (i.e., in reflection mode but focalized on a small thickness of an advanced insulation material).

The rest of the manuscript is organized as follows. In Section 2, a description of the multilayer specimen is given, followed by the modality of acquisition of thermal images in Section 3. Section 4 describes how the numerical model was built and the main results obtained, whereas in Section 5 the innovative FIF2 pre-processing tool is presented. Section 6 focuses on the description of the post-processing techniques, performance measurement procedure, and discussion of the experimental results.

Section 7 validates the numerical part with an experimental procedure based on the Parker method. Finally, Section 8 ends the paper with conclusions.

2. Materials

The multi-layer material studied in the following is similar to the so-called ETICS - External thermal insulation composite system, but, in the case presented in this work, contains a different kind of finishing coating that includes hemp fibres. Therefore, the name of the layers differs a bit with respect to the usual designations, i.e., expanded polystyrene (EPS), base coat reinforced with an embedded glass fibres mesh, finishing coating, to underline the evolution of the product.

The specimen consists of a bearing base of styrofoam (insulating material), with a layer of cement milk superimposed on this surface. A fibreglass reinforcement mesh (thereafter called grid) is embedded in the cement milk layer. The latter aims to homogenize any mechanical stresses that may start on the styrofoam towards the finishing layers. Stresses of thermal nature also cause inevitable expansion effects, which determine deformations in materials containing different layers, like the one under investigation. The fibreglass grid allows to homogenize of surface tensions. The choice of this material is not only due to technical requirements (the grid is indeed very flexible and follows any irregularity during installation); in addition, it is not subject to oxidative phenomena. Superimposed to the grid there is a layer of cement mortar. This layer was not applied for the entire length of the specimen, leaving an area of the reinforcement grid not covered. This choice allows evaluating the thermal insulation effects offered by the cement mortar in addition to the remaining underlying stratigraphy of the specimen schematized by a numerical model. Above the cement mortar, there is the last layer of hemp fibres. This layer has an area of 7.5 × 11 cm. Similar to the construction solution designed for cement mortar, it allows highlighting the thermal insulation effect of the hemp fibres compared to the remaining underlying layers. The detailed description of the stratigraphy in terms of thickness and thermophysical properties is shown in Table 1, see [29] for more details.

Table 1 – Technical and thermophysical properties of the materials under analysis. The last column on the right side represents the porosity in terms of volume percentage. The number n. of each material, specified in the left most column, corresponds to the number shown in Fig 1a.

n.	**Material**	**Thickness** *m*	**Conductivity** *W/mK*	**Density** *kg/m³*	**Specific heat** *J/kgK*	**Emissivity** *ε*	**Porosity** *[%] Vol.*
1	Scattered Hemp Fibres	0.001	0.038	25	1700	0.9	0.120
2	Cement mortar	0.0005	1.73	900	0.21	0.54	0.22
3	Fibreglass	0.0002	0.035	21	1030	0.75	0.44
4	Cement milk	0.0001	1.4	1540	0.87	0.92	0.147
5	Expanded Styrofoam	0.0286	0.03	30	1450	0.6	0.497

In Fig. 1a, a picture of the specimen taken from different angles is shown, while in Fig. 1b an image of the numerical model of the whole specimen is depicted. The numerical model inherent to the specimen was numerically analyzed via the work-plane technique.

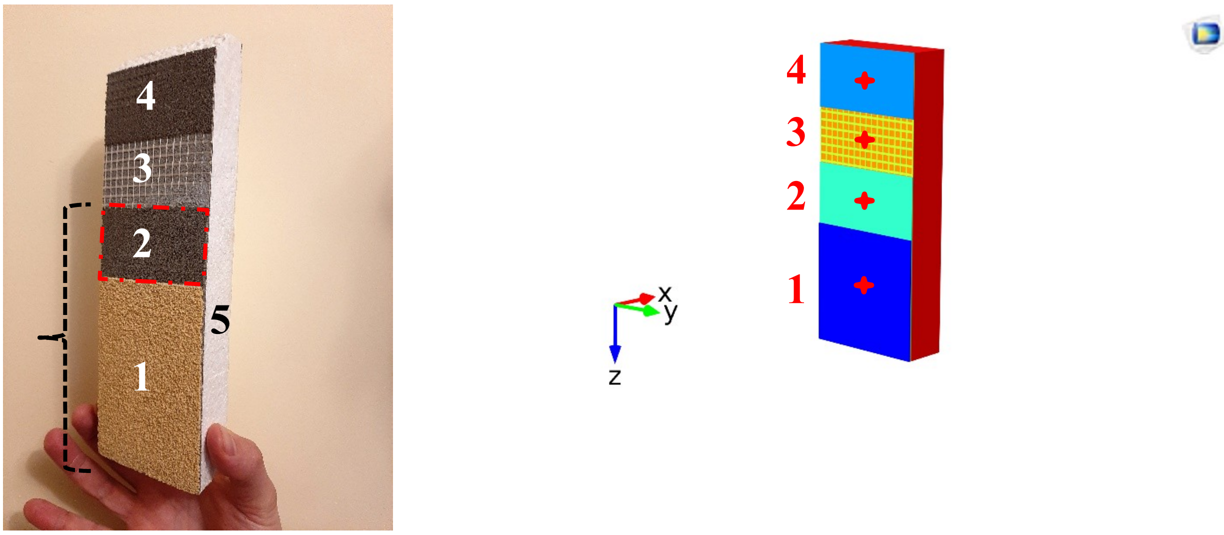

a) b)

Fig. 1: Specimen: a) photograph showing the five most important areas, and b) the numerical model representation of the whole specimen. In Fig. 1a, the red dash-dot rectangle highlights the grey area 2 (i.e., the acquamarine in Fig. 1b), where the grid is hidden under one layer of material. The yellow area 1 (hemp fibres – i.e., the dark blue in Fig. 1b) is where the grid is hidden under two layers of material. The centroids (subsequently explained) of each sub-area are highlighted with a red cross.

With reference to Fig. 1a, it should be noted that the following numerical modelling part, Section 4, is focalized on the entire specimen **surface constituted by four areas, while the experimental part, Sections 5 and 6, is focused only on areas 1 and 2 identified by a brace. Given the thickness of these two areas, they represent the worst-case to detect the subsurface grid.**

3. Acquisition of thermal images

In order to study the behaviour of the specimen, the latter was placed on a wooden support at low thermal conductivity. This to avoid local conduction effects at the contact surface. Fig. 2 shows the testing scheme, including the thermal sources, which have a truncated cone shape. These devices generated a controlled thermal load on the surface of the specimen itself. The thermal camera (FLIR S65 HS, 320 × 240 pixels, 7.5 – 13 μm) was placed in the middle of the headlamps to capture the trend of the thermal evolution, which develops on the surface shown in the left most panel of Fig. 1a, in the most homogeneous way possible.

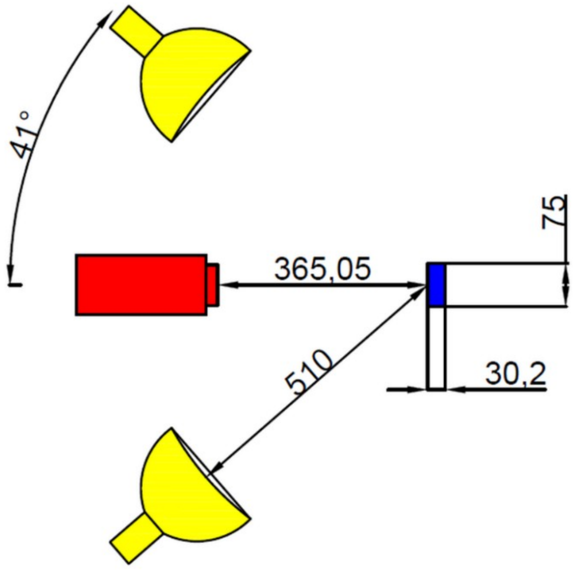

Fig. 2: Testing scheme in the laboratory.

The projectors were equipped with Siccatherm® Osram 250 W lamps.

4. Numerical modelling

4.1. Detail of the model

Firstly, based on literature data [32], a numerical model of the lamps was reproduced. Through the Catia V5® software, the geometry of the lighting body was built in terms of bulb and filament. Subsequently, the geometric model was imported into Comsol Multiphysics® software.

Starting from the electric power developed by the filament (known from the nameplate) and having selected tungsten as its constituent, the electric load was modelled. An electric power supply with known characteristics was numerically simulated, which generated heating of the lamp for a time of 120 s. The subsequent evolution without activated electric power lasted 510 s. The latter step was necessary for the analysis of the cooling thermal transient regime. This allowed mapping of the temperature range of the lamp – on the projective surface of the bulb – for both the heating and the cooling phases. In particular, the numerical simulation of the cooling phase allowed to evaluate the evolution of the surface temperature of the lamp bulb. This step allowed also to understand the effect of the thermal inertia of the lamp otherwise not determinable except by experiment.

When the electrical load ends, in fact, the lamp leads to a decrease in its surface temperature as a function of the thermophysical conditions of the surrounding air. In our case, natural convection replicating the real thermophysical conditions of the test was modelled, i.e. T = 293.15 K, and relative humidity (RH) = 50 %. The latter values were established through a thermohygrometer.

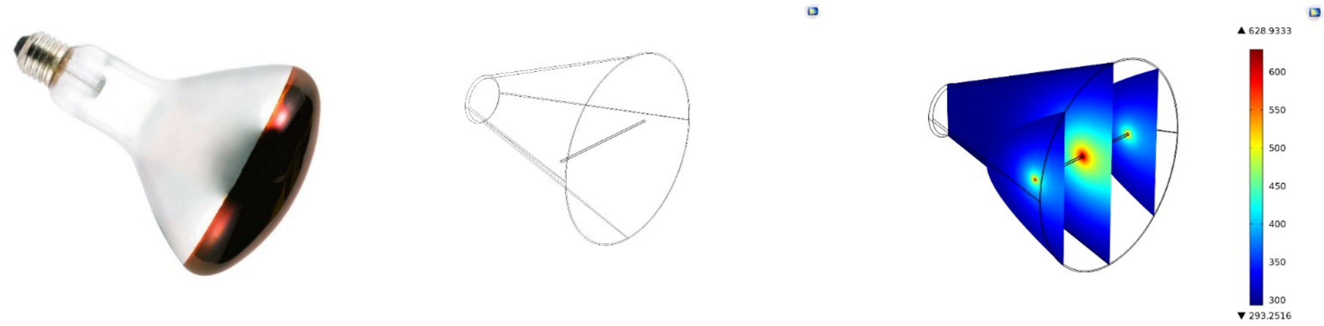

a) b) c)

Fig. 3: Images of the truncated cone lamp: a) photograph, b) model, c) trend of temperature field on three orthogonal slice planes along the filament for a generic temporal instant of the heating phase.

Fig. 3a shows an image that highlights the geometry of the lamp. Fig. 3b presents the reconstructed geometric model. Finally, in Fig. 3c, a salient image of the numerical calculation model is depicted.

In particular, the temperature field for a generic time instant of the heating phase is shown in Fig. 3c. The purpose of this figure is to show to the reader that the analysis of the surface thermal field was obtained, not only by evaluating the effects of radiation, but also by calculating the convection effects of the gas contained in the bulb of the lamp.

Fig. 4 shows the trend of the temperature field on the projective surface of the bulb of the lamp.

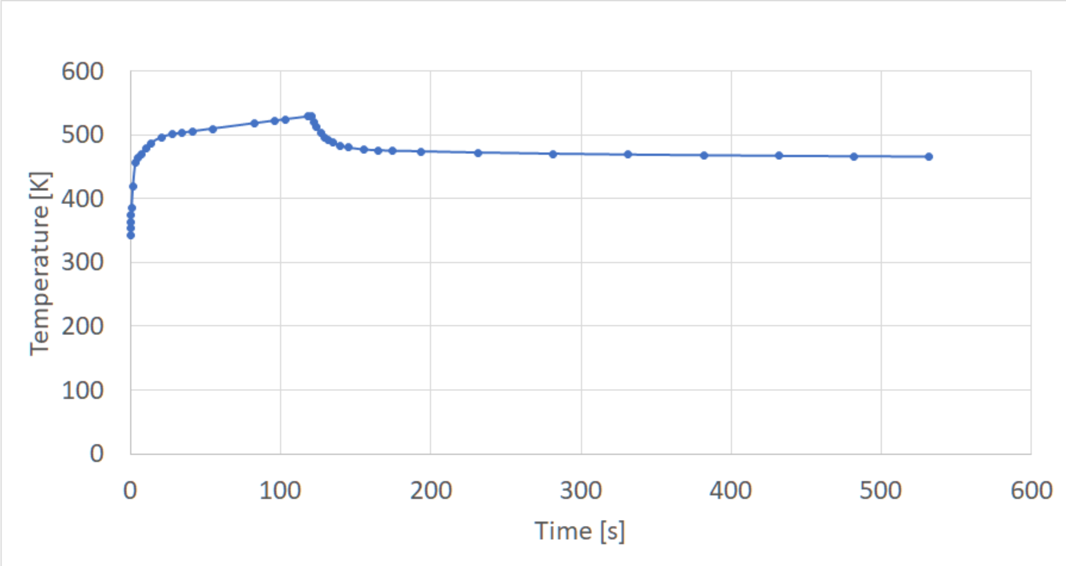

Fig. 4: Trend of the temperature field on the projective surface of the bulb of the lamp.

The temperature profile of Fig. 4 is necessary as an input, saved in data format, to the final model for the study of the evolution of the temperature range of the specimen.

The overall model, in fact, provides only for the insertion of the heat load law of the projectors, instead of the physical elements. This technique allows to reduce the computational cost for a couple of aspects, i.e.:

- a mesh is not necessary for the discretization of the projectors;
- the multiphysics must deal only with the coupling between the input forcing (as data format) and the evolution of the energy transmitted in the form of heat into the specimen.

By carefully observing the two aspects described above, it is evident, first of all, that the projectors do not require any further geometric representation/clarification, since they were studied in the previous model. Secondly, the multiphysics does not have to couple the energy conversion between electrical and thermal load at the same time, but it will only have to deal with the effect that the thermal forcing exerts on the specimen.

From the modelling point of view, in the 3D geometric model, two projectors were considered as punctual elements in the space. The centroids of the projectors represent the absolute position, and the temperature law calculated with the previous model is imposed at these two points.

Subsequently, the software calculated the view factor and the mutual effects between projectors and specimens. The overall model foresees the realization of the geometry using Catia V5®, faithfully replicating the real topology of the model. Then, the geometry was imported into Comsol Multiphysics® software as shown in Fig. 1b.

The selection of the mesh of the specimen was particularly difficult in this case. In fact, even though the external dimensions (parallelepiped) and the thicknesses of the layers making up the model are regular, it was not possible to use of a swept mesh. The presence of a reinforcing grid which does not have contact with any upper layer for a certain extension of the specimen, in fact, made impossible the use of a swept mesh, since there was no correspondence in terms of the number of nodes between the top and bottom surfaces. The meshing procedure on the grid constrained the choice of a tetrahedral mesh. Given the geometric dimensions of the grid, a nodal thickening of 0.0001 m and a resolution of narrow regions equal to 0.25 were necessary. These values were obtained through a series of iterations to evaluate the most efficient refinement while minimizing the computational cost. The meshing process was complex also for the cement milk layer. The insertion of the warp and weft of the fibreglass inside the cement milk resulted in the formation of a series of parallelepipeds having a square base which appeared to be the negative of the footprint of the grid itself. The mesh of the cement milk, therefore, required the same degree of accuracy as fibreglass. Given the regularity of the bottom of the layer (single parallelepiped), it was possible to reduce the number of nodes by controlling the *maximum element grow rate* parameter along the *x* vector (i.e., the depth). For the remaining layers, the mesh was built thanks to the automatic process. The model as a whole has several nodal elements equal to 372346 element domain, 132258 boundary domain, and 28150 edge domain. Considering both the required multiphysics and the number of degree of freedom (DOF) to be solved, it was almost impossible to calculate the necessary numerical model with an ordinary personal computer (PC). Considering a storage capacity of 16 Gb, for the selected multiphysics it was necessary to reduce the number of nodes to a maximum of 3×10^6 as described in the graph titled *Memory requirements (with a second-polynomial curve fit) with respect to degrees of freedom for various representative cases* [33].

The problem could be solved through the specular surface geometry of the specimen with respect to the plane of symmetry *xz,* ref. Fig. 1b. At this point, it was necessary to make a "numerical" cut of the model by defining a work plane that virtually transects the geometry into two mirrored parts. Through the *partition object* controller, it was possible to separate the numerical part into two analysis parts. Two distinct approaches could be followed at this point:

- the first approach is solving the first half-part of the model and, subsequently, the second half-part by coupling them;

- the second approach is solving only one semi-part of the model, mirroring the solution. This second approach requires, however, an appropriate analysis of the boundary conditions.

The latter approach was followed herein. Since the specimen was in contact with the environment, whose boundary conditions do not vary on its sides, it was possible to set natural convection and irradiation conditions on the whole model except for the virtual side named *work plane*. The material continuity boundary condition was set on the *work plane*.

This was necessary to obtain a homogeneous temperature field behaviour at the union interface between the two half-parts. In Comsol Multiphysics® software, the settings that allowed these conditions were the *Continuity on Interior Boundary* $-n \cdot q = q_0 \, on \, \partial \Omega$ (where: $\boldsymbol{q}$ is the conductive heat flux vector (W/m^2), $\boldsymbol{n}$ is the normal vector out at the surface under analysis, q_0 is the inward heat flux (W/m^2), and Ω is the frontier of the layer domain) for radiative effects (using the Rosseland approximation) and the *thermal insulation* $n \cdot (k \nabla T) = 0$ *for conductive effects*.

This allowed to obtain a continuity of the homogeneous thermal field before and after the *work plane*. The physics set both for the numerical solution of the projector and the overall model was the *Heat*

Transfer with Radiation in Participating Media. Concerning the projector, the *Heat Transfer in solids* (which was responsible for evaluating the heat transfer on the materials in the solid-state of aggregation, e.g. the lamp bulb) was on the basis of the physics (Eq. 1).

$$\rho C_p \frac{\partial T}{\partial t} + \underbrace{\rho C_p u \cdot \nabla T}_{1} = \nabla \cdot (k \nabla T) + Q + Q_r \tag{1}$$

Where ρ, indicates the density in kg/m^3, Cp the specific heat at constant pressure J/kgK, T the temperature in K, u represents the velocity field tensor m/s (here, the term 1 of Eq. 1 is null because the components are mutually immobile), Q indicates the source/sink of heat expressed in J, and Q_r is the heat source / radiative sink of heat expressed in J.

Regarding the aeriform (i.e., the internal protection gas of the bulb) the *Heat Transfer in fluids* function was used (Eq. 2).

$$\rho C_p \frac{\partial T}{\partial t} + \underbrace{\rho C_p u \cdot \nabla T}_{1} = \nabla \cdot (k \nabla T) + Q + Q_r + Q_{vd} + Q_p \tag{2}$$

Eq. 2 differs from Eq. 1 for the term 1 which, in this case, is not null due to the convection effects of the fluid, as well as for the heat Q_{vd} of the viscous dissipations J and, lastly, for the heat Q_p due to the effects of the pressure load J. On the other hand, the overall model is governed not only by Eq. 1 and Eq. 2, but also by Eq. 3, which regulates the radiative effects coming from the projectors.

$$\underbrace{S_i \cdot \nabla I_i}_{1} = \underbrace{k I_b(T)}_{2} - \underbrace{\beta I_i}_{3} + \underbrace{\frac{\sigma_s}{4\pi} \sum_{j=1}^{N} \omega_j I_j \varnothing(S_i, S_j)}_{4} \tag{3}$$

The term 4 of the Eq. 3 shows the presence of a discretization of the angular space; usually, the term 4 is presented in the integral form extended from $0 \rightarrow 4\pi$ to analyze all directions. In our case, since there were only two projectors that imposed the thermal load, the term 4 degenerated into numerical quadrature of discrete directions. In Eq. 3, the summation has upper term N, which corresponds in the present case to 2. In particular, the term 1 of Eq. 3 represents the radiative intensity gradient I as the *i-th* component projected in the S direction. Regarding term 2 of Eq. 3, the letter k is the absorbed fraction of the radiative intensity evaluated for the black body $I_b(T)$. In term 3 of Eq. 3, the fraction β indicates the radiant intensity

I_i with respect to the generic *i-th* direction. The term 4 of Eq. 3 is inherent to the scattering coefficient σ_s divided by 4π as the function is spatial. The remaining part of Eq. 3 term 4, the summation, indicates the phase function, which evaluates the probability that a generic ray from the direction S_i is projected in the direction S_j. The definition of the phase function depends on the material constituting the single layer, while the ω_j term indicates the *j-th* direction. To allow the overall numerical model to incorporate the effects of the projectors and the surrounding air, which are not included in the model, the Rosseland approximation should be introduced. The Rosseland approximation assumes that the coupling medium (both the air surrounding the model, and the air between the lamp and the projector box) is optically dense. Calling τ the optical thickness, this must assume a value $\tau >> 1$. More precisely, by defining the integral of the absorption coefficient, κ along a typical optical path S, Eq. 4 can be written:

$$\tau = \int_0^S \kappa ds \tag{4}$$

From the modelling point of view, this approximation has a very limited impact (in terms of computational cost). In fact, it does not introduce any further degrees of freedom into the heat equation. Conversely, it adds a non-linear contribution to thermal conductivity. Therefore, the method here explained is widely used. In fact, it avoids representing physically in the numerical model media whose optical thickness is high. However, since it provides a simple approximation of heat transfer by radiative effects in coupling media, it must be used carefully. In particular, the fraction of radiative heat Q_r coming from the interaction of the thermal beam and the coupling air medium is evaluated following the relationship shown in Eq. 5.

$$Q_r = \frac{4\pi}{\beta} \nabla I_b \tag{5}$$

Where the symbols of Eq. 5 have been described previously.

Also, the fluid dynamic model for the coupled analysis of radiative and convective phenomena requires a specific package of Comsol®, i.e. *the laminar flow*, integrated with a dedicated multi-physics. The latter deals with correlating the radiative effects with the convective ones. The set of governing equations of this package includes the conservation mass equation in the conservative form (Eq. 6) and the compressible flow equation (Eq. 7), respectively.

$$\frac{\partial \rho}{\partial t}+\nabla\cdot(\rho u)=0 \quad (6)$$

$$\rho\frac{\partial u}{\partial t}+\rho u\cdot\nabla u=-\nabla p+\nabla\cdot\left(\mu\left(\nabla u+(\nabla u)^T\right)-\frac{2}{3}\mu(\nabla\cdot u)I\right)+F \quad (7)$$

Where ρ is the density in kg/m^3, μ is the dynamic viscosity in $Pa{\cdot}s$, $\boldsymbol{u}$ is the velocity in m/s, p is the pressure in Pa, $\boldsymbol{F}$ is the volume force vector N/m^3.

In the following, a spherical integration domain – for the fluid dynamics part only – was selected. This choice was dictated by the lower computational cost that a sphere requires with respect to the cube domain. This was made possible by the geometry of the multilayer that has the measurements of the same order of magnitude. The cubic domain – used in the case of thermal analysis of the specimen only – is larger respect to the fluid dynamics domain of the air medium representing the spherical domain. The spherical domain, in fact, is a subdomain of the cubic one. Therefore, the calculation of the number of nodal elements for the mesh is simplified and, at the same time, the spacing of the nodal elements near to the boundary domain is optimized. Also in this case, the lamps were not considered because, as mentioned previously, they were useful to the modeller only for the forcing as well as for the thermal inertia in the form of external body (i.e., not as a Dirichlet condition on the surface of the multilayer).

The real complexity of the convective calculation lies exclusively in the evaluation of the coefficient h. In fact, a functional relationship that links the convective exchange coefficient to some physical quantities related to the analysis already exists. The relationship of interest is reported in Eq. 8.

$$h=f(\lambda,\rho,C_p,\mu,L,w_\infty) \quad (8)$$

where λ is the thermal conductivity W/m^2K, ρ is the density kg/m^3, C_p is the specific heat kJ/kgK, μ is the dynamic viscosity kg/ms, L is a geometric parameter dependent to the geometry and expressed in m, and w_∞ is the velocity of the fluid in undisturbed conditions in m/s. Bearing in mind the multitude of parameters on which h strictly depends, its determination is complex. To reduce the independent variables to be analyzed, dimensionless groups are introduced (including Nusselt, Grashof and Reynolds) to study the fluid distribution in space. The Nusselt and Reynolds numbers are of particular interest for this study. The first is a ratio between the amount of heat exchanged by conduction and the amount of heat exchanged by convection, while the second is the ratio between the forces of inertia and the viscous forces. The former can also be determined through other dimensionless groups through empirical relationships among which the famous Mc Adams's relation for vertical flat surfaces that functionalizes Nusselt as follows.

$$Nu = C\,Gr^{a}\,Pr^{b} \tag{9}$$

Where for $R_e < 10^9$, the terms C, Gr and Pr represent a constant value depending on the geometry of the problem under analysis, the Grashof number and the Prandtl number, respectively. The exponents a and b are empirical coefficients related to the system under analysis. However, having a modelling software it is possible to express the Nusselt number differently by purifying it from the empirical coefficients, which are certainly more suitable for a generic problem than for a specific case. For this, a specific variable was created in Comsol® Nusselt Variable that calculates the trend in the integration domain thanks to Eq. 10.

$$\frac{\left(\dfrac{3\,D\,domain\,convective\,heat\,flux\left[\dfrac{W}{m^{2}}\right]}{3\,D\,local\,point\,domain\,temperature\,[K]}\right)\cdot minimum\,specimen\text{¿}\,[m\text{¿}]}{3\,D\,domain\,mean\,effective\,thermal\,conductivity\left[\dfrac{W}{mK}\right]} \tag{10}$$

In this way, thanks to the variables inside the code, it is possible to go back to the Nusselt value without the use of empirical coefficients. As for Prandtl, there is already a variable implemented in the code. Thanks to the Number and Prandtl numbers it is possible to have a whole scenario of the influence of convection on the model under analysis. To show the trend of the Reynolds and Prandtl numbers, the readers may refer to Fig. 5.

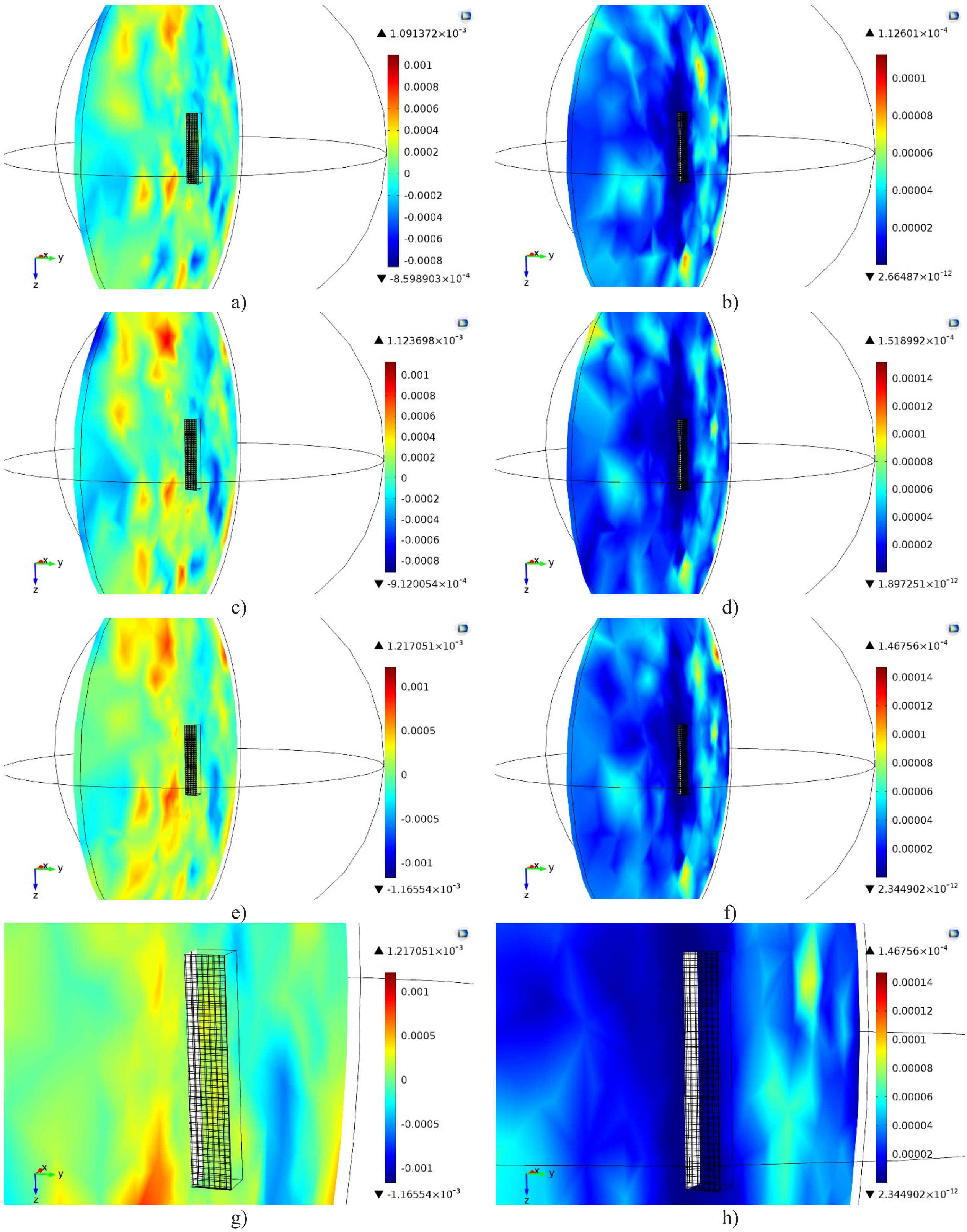

Fig. 5: Calculated trend of the dimensionless Reynolds and Nusselt numbers: a) Nusselt at 100 s, b) Reynolds at 100 s, c) Nusselt at 300 s, d) Reynolds at 200 s, e) Nusselt at 300 s, f) Reynolds at 300 s, g) magnification in the proximity of the specimen with respect to a generic instant of time for the calculation of the Nusselt number, and h) magnification in the proximity of the specimen with respect to a generic instant of time for the calculation of the Reynolds number.

In the spherical domain shown in Fig. 5, the trends of both the Reynolds number and the Nusselt number were calculated for some instants of time of interest. In particular, the Figs. 5a, c and e, show low Nusselt values centered around zero. Bearing in mind that the thermophysical properties of the experimental test have infinitesimal variations – except for the surface temperature of the specimen –, the heat transfer coefficient has a direct proportionality to the Nusselt number. It is obvious that for an energy transfer coefficient in the form of negative heat, the Nusselt number will be negative accordingly. The fact that the Nusselt number is perfectly centered with respect to zero, it agrees with Figs. 5b, d and f that show a very low Reynold number typical of natural convection in still air. Figs. 5g and h show magnifications in the proximity of the specimen, while the blank area shows that the computation domain is only on the fluid, and this underlines the numerical correctness of the model.

4.2. **Results and Discussion of the numerical part**

The heated specimen is shown both in Fig. 6 and in Fig. 7 for the heating up and cooling down phase, respectively.

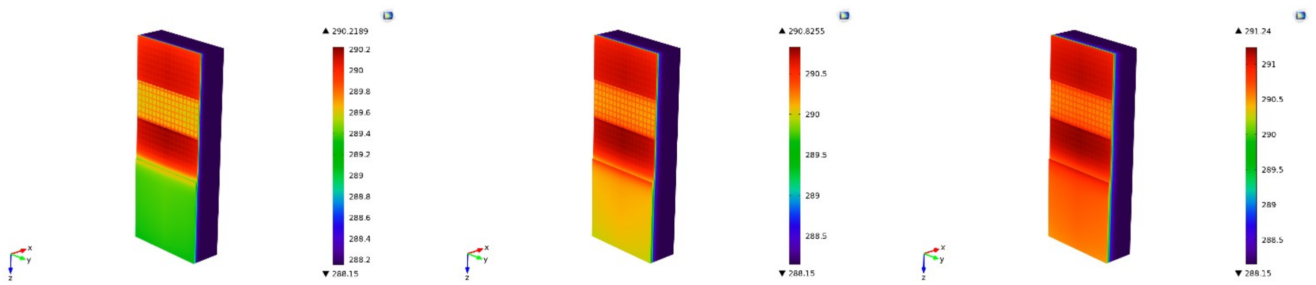

a) b) c)

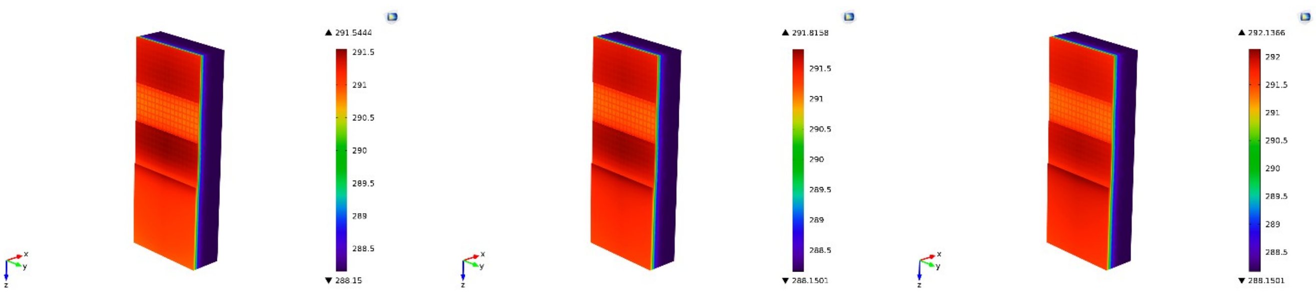

d) e) f)

Fig. 6: Trend of the heating phase of the specimen registered after: a) 10 s of heating, b) 20 s of heating, c) 30 s of heating, d) 40 s of heating, e) 80 s of heating, f) 120 s of heating.

Fig. 6a shows how the thermal field is characterized by a temperature range of 1.2 K on the surface of the specimen. In particular, the area less sensitive to thermal load is the one inherent to the hemp fibres (i.e., the yellow area in Fig. 1). The insulating effect of this layer compared to the layer of cement mortar near to it is evident. It is possible to notice the presence of the grid under the layers of the cement mortar. It is interesting to see how the correct setting of the boundary condition of the numerical model can be verified precisely from the corners at the top right and the top left. The right approach undertaken is made evident both by the symmetry of the temperature field and by the non-homogeneous trend of the temperature field near the right and left vertices.

In Fig. 6b, it is possible to notice a homogenization of the temperature field on the front surface, while the thermal gradient between the points of it goes up to 1.8 K. The grid beneath the cement mortar gradually becomes less evident; this fact is due to the homogenization of the temperature value between the surface layer and the remaining subsequent layers.

In Fig. 6c the homogenization of the temperature field on the surface is shown. The temperature gradient on the surface is ~1 K, and the reinforcement grid inside the cement mortar layer becomes less and less evident. On the other hand, it is interesting to note how the thermal diffusion of the fibreglass is such that its surface temperature value does not quickly adapt to the temperature value of the layer that contains it. Although the latter is particularly thin (the thickness of the fibreglass is 0.0002 m), the texture of the grid appears clearly both inside the layer of cement milk, and beneath the layers of cement mortar.

In Fig. 6d, it is possible to notice a further homogenization of the surface temperature field, with a surface gradient of ~1.5 K. The reinforcement grid is less and less visible beneath the layers of cement mortar. It is evident that the homogenization tends to occur also for the reinforcing grid inside the cement milk.

Fig. 6e shows that the homogenization process of the thermal field completes its process of diffusion over the entire surface layer. The surface temperature gradient between the points at the greatest difference is ~1.1 K, while through the thickness there is a maximum gradient of 4.46 K. It is still possible to distinguish the position of the reinforcement grid for the cement mortar layers.

In Fig. 6f, the reinforcement grid is almost completely homogenized in the cement milk layer. The temperature gradient between the points of the surface layer at the greatest difference is ~1.3 K. The trend along the *x* vector, which appears homogeneous and uniform despite having an additional layer of hemp fibres (i.e., the yellow area (1) in Fig. 1a), is of particular interest. Regarding the trend of temperature gradient through the thickness, a value of ~5.2 K can be detected.

As previously said, Fig. 7 shows the trend of the cooling phase of the specimen.

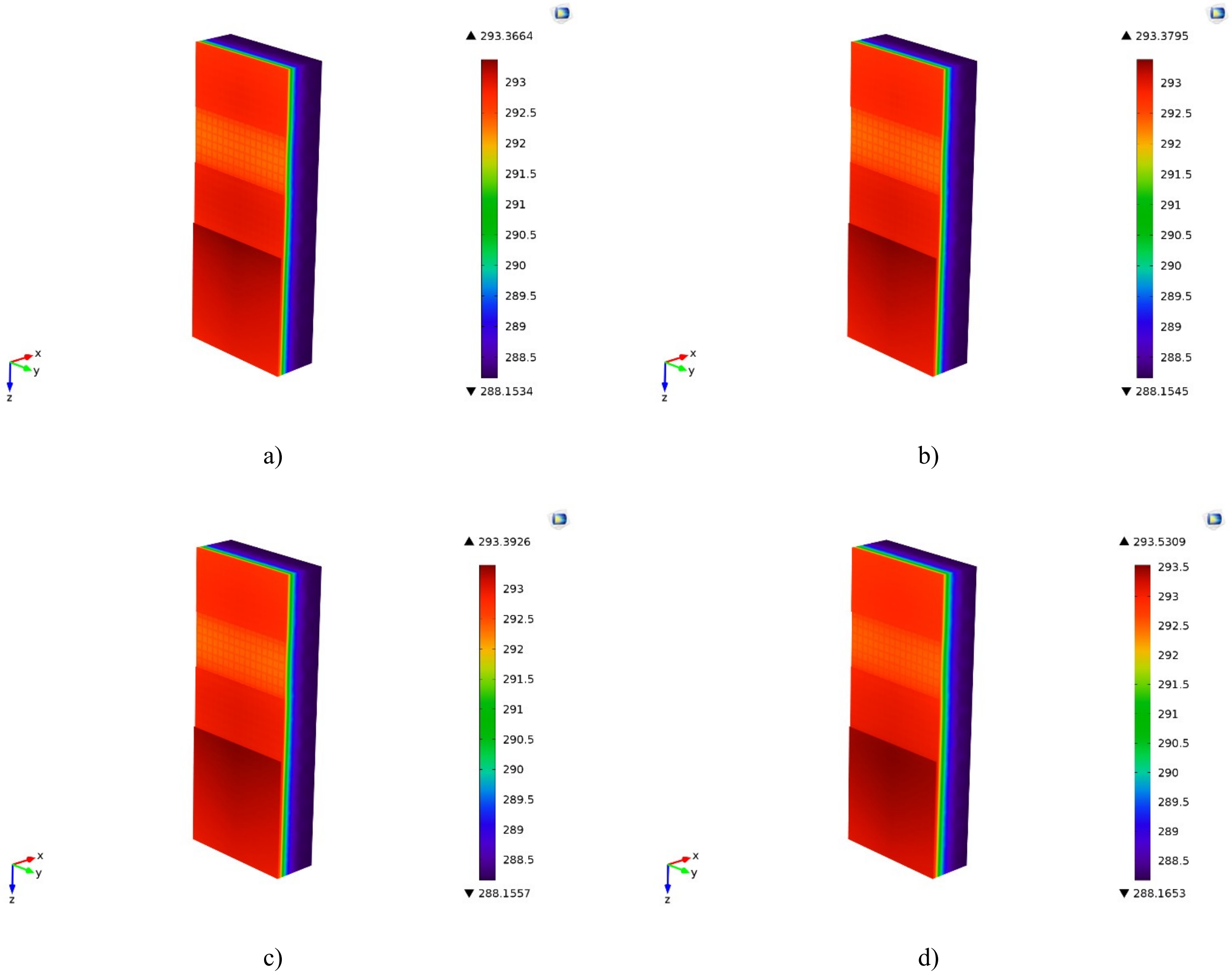

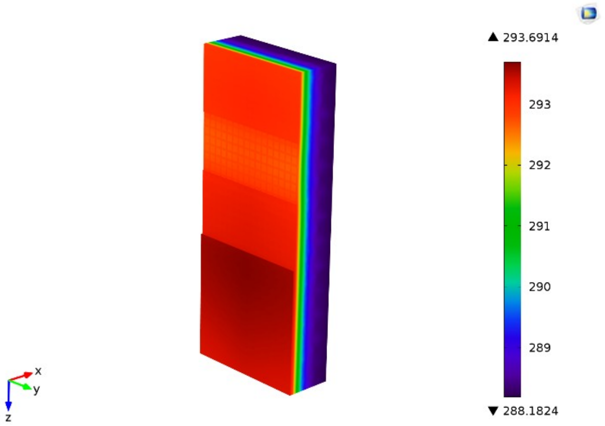

e)

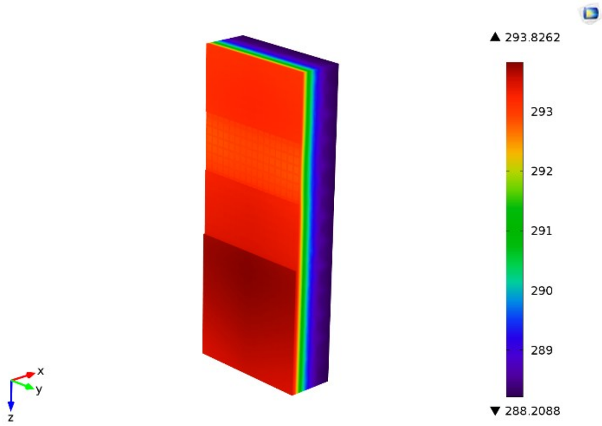

f)

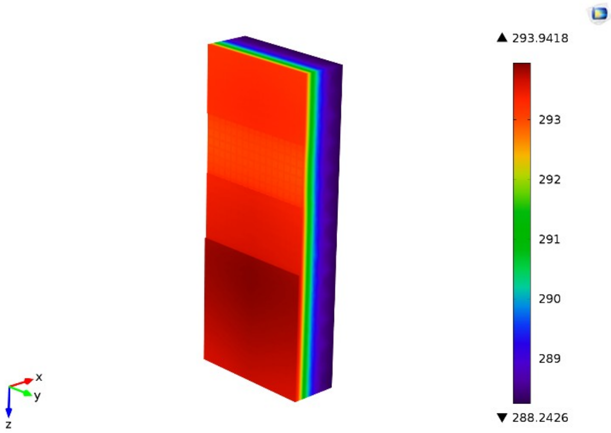

g)

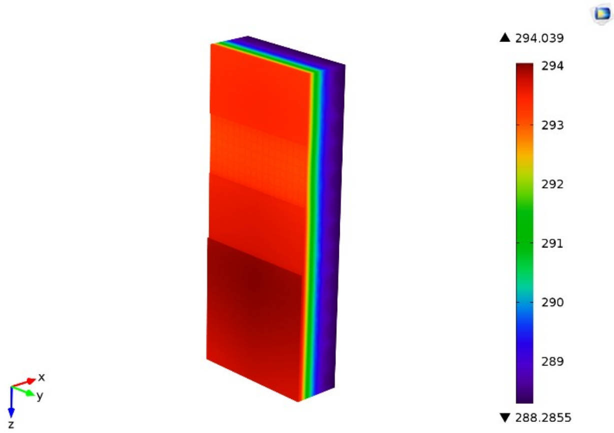

h)

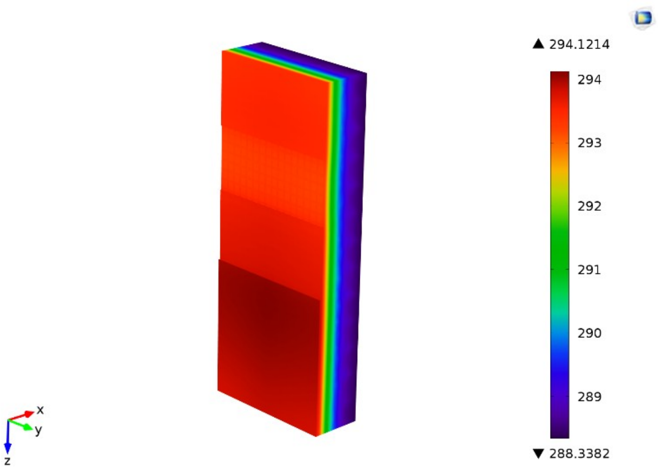

i)

Fig. 7: Trend of the cooling phase of the specimen registered after: a) 10 s of cooling (130 s from the beginning of the experiment), b) 20 s of cooling, c) 30 s of cooling, d) 80 s of cooling, e) 180 s of cooling, f) 280 s of cooling, g) 330 s cooling, h) 380 s cooling, i) 390 s cooling.

Fig. 7a shows how the numerical model also calculates the effects of thermal inertia due to the cooling of the projector plus the thermal release that the material making up the specimen undergoes. The considerable reduction of the thermal load when the projector turned off led to a lowering of the surface temperature of the specimen. This condition highlighted the reinforcement grid beneath the mortar layers which was not visible at maximum heating (Fig. 6f).

The area of the specimen not covered by cement mortar also makes the grid more evident than in Fig. 6f. In Fig. 7b the *thermal imprint* of the reinforcing grid appears slightly detectable also on the hemp fibres layer, above all for the area proximal to the cement mortar. This is of great interest by considering the experimental results described in sub-section 6.2.

It is possible to observe that the temperature gradient equal to ~1.3 K remained unchanged on the frontal plane. Even after 20 s of cooling, the temperature difference on the surface was almost like during the heating phase. This is due to the strong characteristics of insulation on which the specimen is based on.

In Fig. 7c the reinforcing grid in the upper zone of the hemp fibres layer is imperceptible. In addition, the grid beneath the cement mortar layer is difficult to distinguish, while its shape is clear on the cement milk layer.

In Fig. 7d the presence of the reinforcement grid in the cement milk layer remains evident. As the cooling time increased, the layers were homogenized in terms of temperature gradient on the surface; in addition, the grid became less and less visible even on the cement milk (Fig. 7e). Finally, through the thickness a very homogeneous stratigraphy of the temperature field can be seen (Figs. 7f, g). By seeing the upper layer of the cement mortar (Figs. 7f, g), an ellipsoidal shape of the temperature field with higher values than the rest of the layer itself appears at the center. The slight difference is attributable to the edge effects responsible for the further decrease in temperature at the perimeter while maintaining the conditions of the central area at the same temperature (Fig. 7h). A further effect is the presence of the reinforcing grid only at the interface between cement mortar and cement milk. This is linked to the local convective effects responsible for the temperature gradients that one has at the interface of the materials. The same effects are also visible in Fig. 7i. To evaluate the trends of the temperature field through the thickness of the specimen, four directions were identified on the numerical model along the *x*-axis of Fig. 1b. These directions were selected one for each centroid of the areas shown in the same figure (i.e., areas **1**, **2**, **3**, **4**). They highlight the virtual probes with respect to which the temperature trends shown in Figs. 8 and 9 were evaluated.

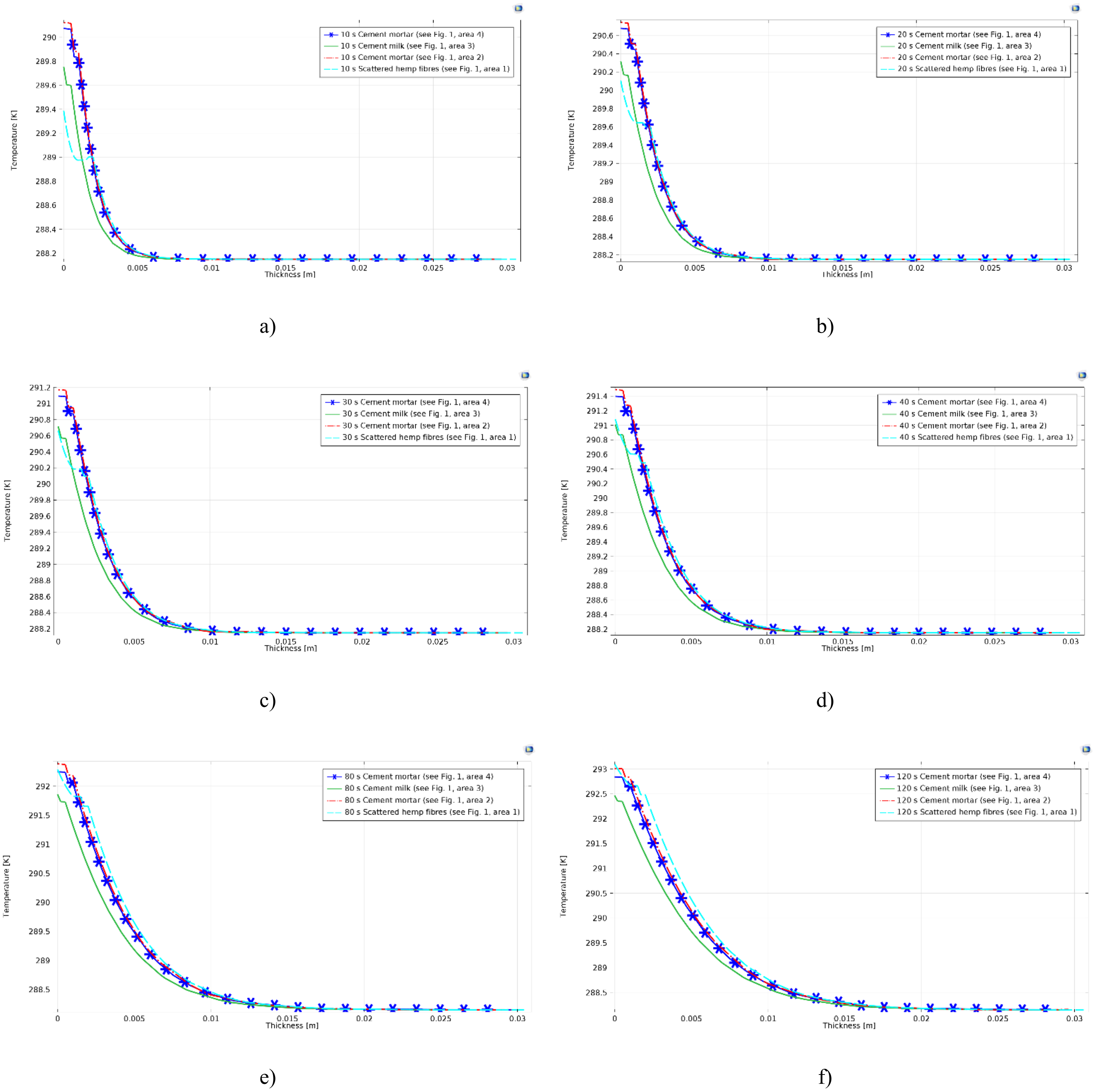

a) b)

c) d)

e) f)

Fig. 8: Temperature trends through the thickness of the specimen during the heating phase after: a) 10 s of heating, b) 20 s of heating, c) 30 s of heating, d) 40 s of heating, e) 80 s of heating, f) 120 s of heating.

As it can be seen in Fig. 8a, the surface temperatures subjected to the same heating (10 s) are not identical for all the materials being analyzed. It is evident that, for the cement mortar, the difference of ~0.05 K is given by the convective effect evaluated by the numerical model. The position of the specimen generated an upward trim tabs effect resulting in a lower surface temperature in the upper part of the model while, in the most central part of the model itself, it is less affected by the convective effects. As for the other layers, they have lower surface temperatures than cement mortar. By carefully seeing the temperature trend of Fig. 8, the maximum surface temperature is reached by the cement mortar directly exposed to the air (see the lowest part of the specimen), followed by the face of the same material at the highest part of the specimen.

The remaining materials facing the lamps, namely, the cement milk embedded in the glass fibres reinforcement grid and the hemp fibres layer were at lower surface temperatures. Hemp is the material that has a lower capacity to undergo an increase in surface temperature, with the same external thermal load imposed. What appears particularly interesting in the temperature trend is the abrupt variation of the first derivative that all the temperature curves have at a depth of 0.0018 m. This thickness is obtained from the sum of the layers of hemp fibres, plus the cement mortar, plus the cement milk, plus the glass fibres grid. Beneath the latter layers, only the styrofoam is present. The temperature trends show differences only for the surface layers. Regarding the trends inherent to the directions of the cement mortar, a uniformity of all the curves can be noticed at the depth of 0.0018 m. Regarding, instead, the temperature trend inherent to the direction of the cement milk, the same slope (slightly out of phase forwards) can be noticed if compared to the remaining layers; this was due to the lower insulating effect of the upper layers. The knee of the curve inherent to the hemp fibres is of great interest. The re-increase in temperature (starting from 289 K drops to 289.98 K to return at 289 K) was due to the thermal inertia of the styrofoam. In fact, the styrofoam layer transfers energy in the form of heat to the area where the hemp fibres layer is to re-balance the temperature. This effect is here visible due to the insulating effect of the hemp fibres. The same effect has occurred for the cement milk, but, since the latter had a higher thermal diffusion than the hemp fibres, it was unable to retain the heat energy. This determined that the green curve in Fig. 8a has followed, without overlapping, the remaining temperature trends. From a thickness of ~0.006 m, all the curves were uniform, which made it impossible to distinguish the various trends.

In Fig. 8b, the trends of the temperature field are very similar to the previous ones, but with a higher surface temperature value. The effect of the temperature knee is always present, but, in this case, a decreasing temperature gradient, with two visible passages with zero derivatives for temperatures 289.62 K and 289.6 K, exists. Since the surface temperature of the styrofoam is higher than the previous case, there is an effect of energy transfer in the form of heat from the external surface towards the styrofoam layer without any reversal.

In Fig. 8c, the effect is similar to the previous case, but the leveling of the temperature curves occurred for a thickness of 0.01 m instead of 0.006 m. Therefore, the temperature equilibrium between the different layers cannot be seen at the interface styrofoam – cement milk, but inside the styrofoam itself.

Fig. 8d shows a trend of the curves like the previous one, but two differences can be highlighted: the surface temperature of the hemp fibres is higher than that of the cement milk; the temperature equilibrium occurred at a depth of 0.012 m within the layer of styrofoam.

In Fig. 8e a change in the temperature field is evident with an alignment of the surface temperatures to a similar value between layers (~291.8 – 292.8 K). The absence of knee is evident for the hemp fibres curve, while the distance between the temperature profiles for the depth between 0.0018 m – 0.01 m stands out. Instead, in the previous case, a more compact trend was found. Furthermore, up to a thickness of 0.016 m there was no equilibrium between the temperature trends. In particular, the thermal equilibrium was not recorded except for the second half of the thickness of the styrofoam layer.

In Fig. 8f, a behavior similar to the previous case can be seen, but it is evident that the surface temperature of the hemp fibres exceeds the other trends. The temperature curves up to a thickness of ~0.02 m have a different slope. Starting from 0.016 m and for the entire remaining thickness, a perfectly equivalent temperature trend is observed on all the different materials included in the specimen.

Fig. 8f is inherent to the maximum heating, whereas Fig. 9 presents the behavior of the specimen during the cooling phase. Fig. 9a shows the trend of the temperature range after 10 s of cooling, i.e., after 130 s since the beginning of the analysis. The trend of the curves is like that of Fig. 8f, but it is possible to notice a difference in the surface temperature of the hemp fibres. The latter grows further by ~0.1 K, even though the heating phase is completed. This is attributable to the thermal conductivity which is lower than that of the materials present on the surface exposed to the thermal load. Therefore, this surface had a reduced propensity for dissipation and the thermal inertia caused here a slight increase in the surface temperature. In addition, all curves tended to maintain the temperature values as in Fig. 8f, but shifted of ~0.001 m towards the face not directly exposed to the thermal load. This effect starts at depth 0.002 m and continuous up to 0.018 m, and it can be attributed to the thermal displacement. Both in Fig. 9b and Fig. 9c, the effects are similar to the previous case with an increase of 0.1 K for every 10 s of cooling.

Also, for the depth temperature trend, the same behavior occurred. These effects are attributed to thermal conductivity, thermal inertia, and typical effects of the phase shift particularly high in materials for thermal insulation.

In Fig. 9d a change in thermal behavior for both the hemp fibres and the cement mortar exists. The surface temperature increased for all the materials by ~0.1 K; however, of particular interest are the curves exploring the thickness of the specimen. These trends are preserved in terms of first derivative and temperature. However, a translation (from 0.018 m to 0.023 m) with respect to the depth that passes from the temperature limit (never modified previously) can be noticed.

In Fig. 9e it is possible to see a change of derivative in the analyzed curves. In particular, through the thickness of the specimen, there is a lower slope of the curves that leads the undisturbed limit of the temperature from 0.018 m (depth) to 0.025 m. This effect balances all temperature trends inherent to the specimen by also increasing the surface temperature by ~0.3 K. In fact, from this moment on, a change in the thermal behavior of the specimen is present.

Subsequently, a progressive linearization of the temperature profiles can be noticed. Obviously, since the specimen has a little thickness, the end of the thermal load starting from 180 s, leads the entire object to thermal equilibrium. It is understandable that the internal energy of the specimen increased during the heating phase, causing, in the cooling phase, an increase in the surface temperatures, which was proportional to the thermal conductivity of the materials constituting it.

In Fig. 9f and 9g, the aforementioned linearization of the temperature curves can be seen, which brings the evolution of the temperature field of the insulating specimen closer over time to generic building material.

In Figs. 9h and 9i, it is possible to notice the cooling conditions at 380 s and 390 s, respectively. Here, the surface temperature tends to become similar for all the layers analyzed and, in particular, there is a difference between the hemp fibres and the cement milk of only 0.5 K. The equilibrium temperature for the face not exposed to the thermal load remained unchanged throughout the test, although it moved to a depth of ~0.029 m. During the analysis of the curves for the entire depth of the styrofoam layer, the trends of the first derivatives changed the modulus of the angular coefficient but never its sign.

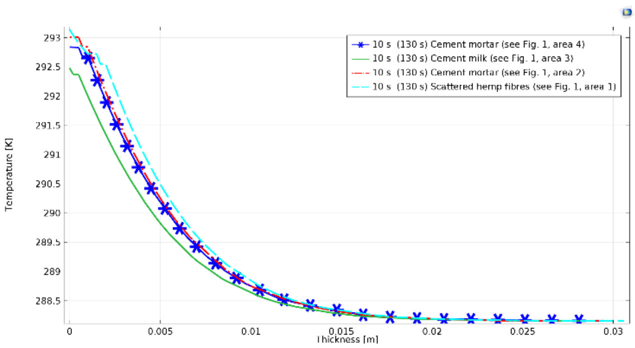

a)

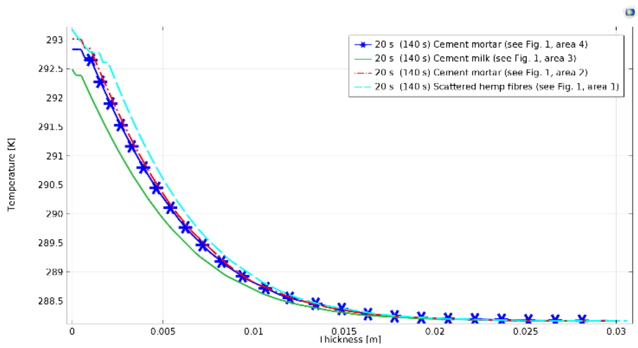

b)

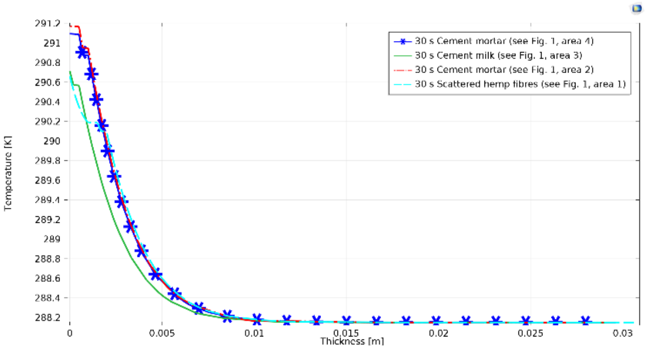
30 s Cement mortar (see Fig. 1, area 4)
30 s Cement milk (see Fig. 1, area 3)
30 s Cement mortar (see Fig. 1, area 2)
30 s Scattered hemp fibres (see Fig. 1, area 1)
Temperature [K]
Thickness [m]

c)

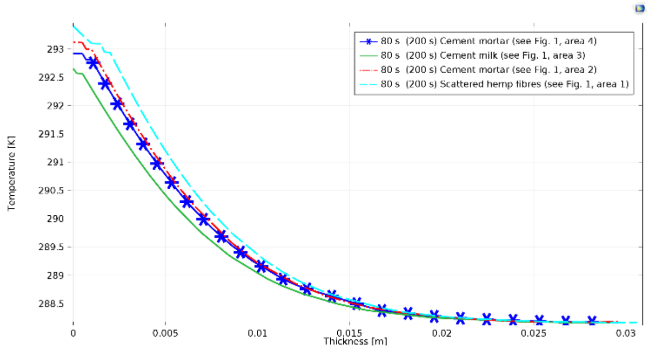
80 s (200 s) Cement mortar (see Fig. 1, area 4)
80 s (200 s) Cement milk (see Fig. 1, area 3)
80 s (200 s) Cement mortar (see Fig. 1, area 2)
80 s (200 s) Scattered hemp fibres (see Fig. 1, area 1)
Temperature [K]
Thickness [m]

d)

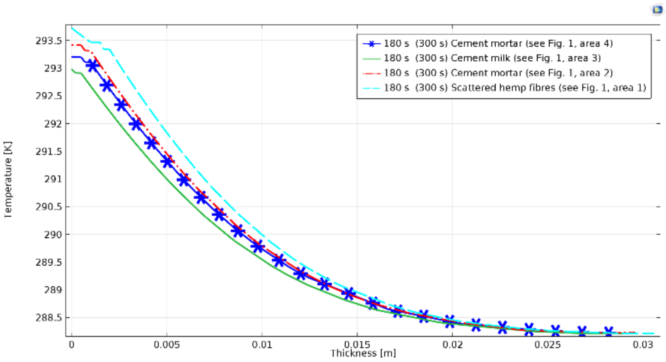
180 s (300 s) Cement mortar (see Fig. 1, area 4)
180 s (300 s) Cement milk (see Fig. 1, area 3)
180 s (300 s) Cement mortar (see Fig. 1, area 2)
180 s (300 s) Scattered hemp fibres (see Fig. 1, area 1)
Temperature [K]
Thickness [m]

e)

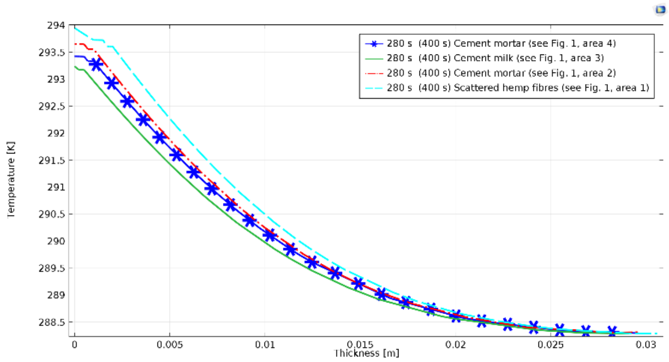
280 s (400 s) Cement mortar (see Fig. 1, area 4)
280 s (400 s) Cement milk (see Fig. 1, area 3)
280 s (400 s) Cement mortar (see Fig. 1, area 2)
280 s (400 s) Scattered hemp fibres (see Fig. 1, area 1)
Temperature [K]
Thickness [m]

f)

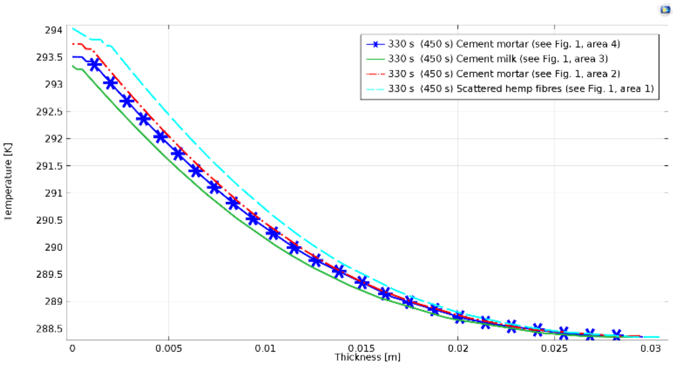
330 s (450 s) Cement mortar (see Fig. 1, area 4)
330 s (450 s) Cement milk (see Fig. 1, area 3)
330 s (450 s) Cement mortar (see Fig. 1, area 2)
330 s (450 s) Scattered hemp fibres (see Fig. 1, area 1)
Temperature [K]
Thickness [m]

g)

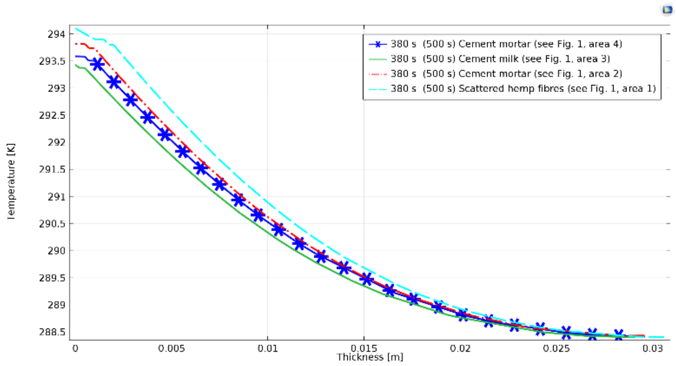
380 s (500 s) Cement mortar (see Fig. 1, area 4)
380 s (500 s) Cement milk (see Fig. 1, area 3)
380 s (500 s) Cement mortar (see Fig. 1, area 2)
380 s (500 s) Scattered hemp fibres (see Fig. 1, area 1)
Temperature [K]
Thickness [m]

h)

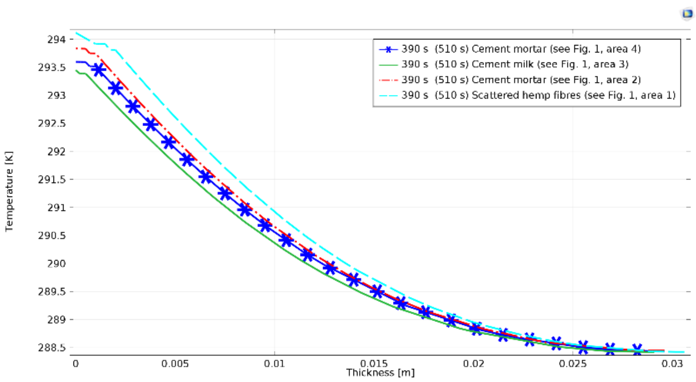
390 s (510 s) Cement mortar (see Fig. 1, area 4)
390 s (510 s) Cement milk (see Fig. 1, area 3)
390 s (510 s) Cement mortar (see Fig. 1, area 2)
390 s (510 s) Scattered hemp fibres (see Fig. 1, area 1)
Temperature [K]
Thickness [m]

i)

Fig. 9: Temperature trends through the thickness of the specimen during the cooling phase after: a) 10 s of cooling (130 s from the beginning of the experiment), b) 20 s of cooling, c) 30 s of cooling, d) 80 s of cooling, e) 180 s of cooling, f) 280 s of cooling, g) 330 s of cooling, h) 380 s of cooling, i) 390 s of cooling.

Since the calculated temperature differences here presented are very small, mostly less than 1 K, a sensitivity analysis (Fig. 10) is provided.

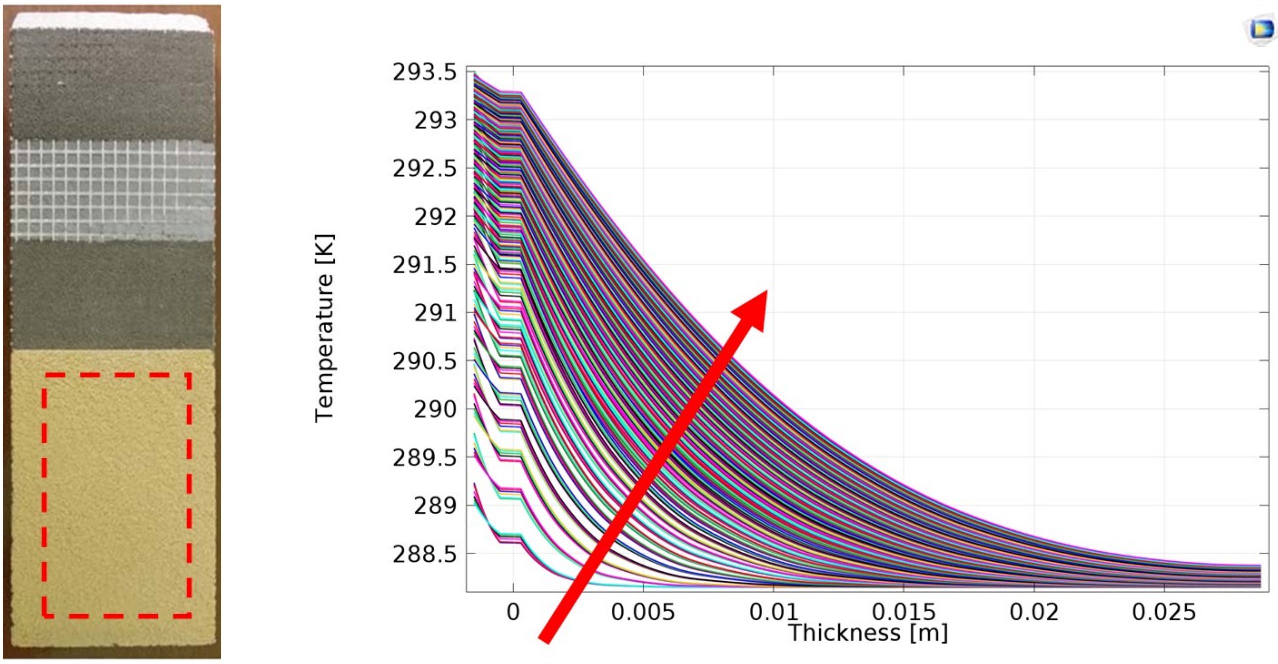

a) b)

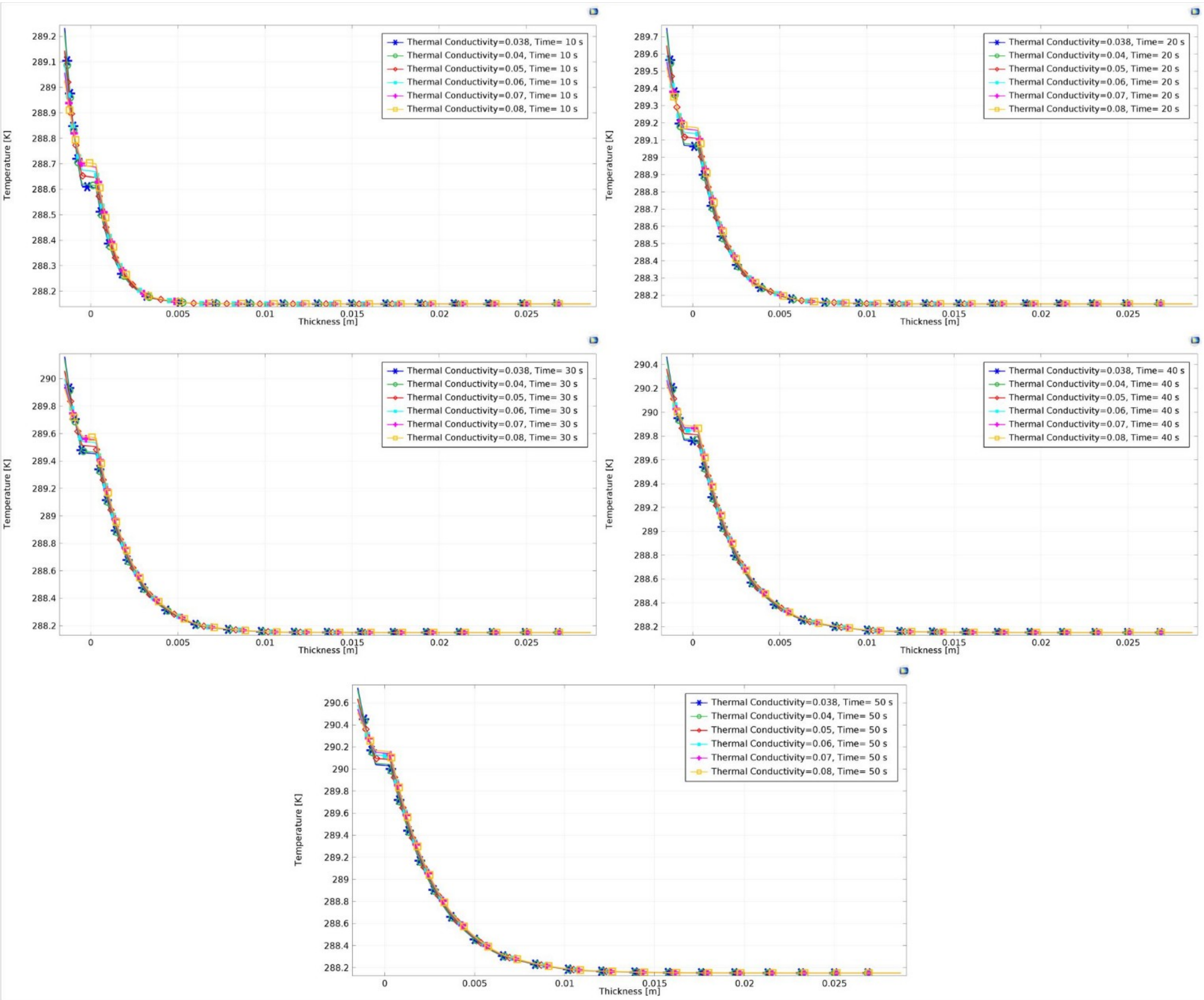

c)

Fig. 10: Sensitivity analysis: a) The red hatch shows the analysis area of the numerical model on which the sensitivity analysis is performed; b) Totality of the temperature trends for all the analyzed thermal conductivity. The red arrow indicates the *compaction direction* of the temperature trends during the time evolution of the numerical model. The reader, by observing the overcrowding of the curves, may note as the calculated time instants increase, the model tends to numerical stability; c) Magnification of the first five temporal moments (Fig. 10b) to evaluate the differences in the temperature field trend for the analyzed thermal conductivity.

It allows to test the response of the numerical model to changes of the input variables. For completeness, the analysis took place on an area of the model having a full stratigraphy (i.e., the dash-dot red highlighted area shown in Fig. 10a). Since, in this case, the thermal load applied predominantly on the expanded styrofoam layer, the sensitivity analysis was carried out by assigning different thermal conductivity values to it, leaving the values of the remaining materials unchanged.

The different values provided in input to the model (only for expanded styrofoam) were: 0.038, 0.04, 0.05, 0.06, 0.07, 0.08 W/mK. The first value (0.038 W/mK) is the real value, while the next five values were selected to test the sensitivity of the model with a variation (in the order of one hundredth) of the thermal conductivity at the input.

In Fig. 10b, the curves obtained for the entire evolution over time of the calculation (i.e., 510 s) are shown. They refer to all the different thermal conductivity values assigned to the first layer, leaving the values of the remaining layers unchanged. The trends do not have the respective legend and, therefore, they are only identifiable in term of general trend and not as a single answer. This choice has two particular reasons, namely: a) trying to explain the behaviors of six different thermal conductivities related to each time instant evaluated in the entire model with an appropriate legend would have required a large number of figures. Just think that the model under analysis, for this figure, contains six curves for 510 time instants (i.e., 3060 curves); b) this graph must serve to understand the stability of the numerical model. In fact, by grouping all the trends into a single graph, the reader may note that the behavior of each single series of curves (generated for each time instant of the respective six thermal conductivities) thickens starting from the base of the red arrow up to the vertex. This ensures that, during the calculated time evolution, the model tends to a stability as visible from the increasingly close temperature trends.

In Fig. 10c, the trends of only the first five time instants have been extrapolated. This in order to show the trends of the curves for the single time instants and, therefore, to understand a little deeper the logic of calculation-comparison used for the study of stability and sensitivity of the numerical model.

It should be noted that the curve at lower temperature is linked with the thermal conductivity having the lower modulus value. In addition, the model appears immediately stable starting from the depth of the second layer. It is evident that the angular coefficients of the temperature curves remain almost unchanged for the layers subsequent to the first, guaranteeing the stability of the response to the calculation of the model. Furthermore, changes in the first layer of thermal conductivity in the order of one hundredth of a W/mK lead to changes in the calculated temperature below 0.25 K. This ensures that the perturbations of the calculated temperature propagate themselves for less than 1/4 K in terms of model response.

5. The 2D Fast Iterative Filtering method as a pre-processing tool

In this section, the authors present a new 2D version of the so-called Fast Iterative Filtering (FIF) method to pre-process the signals under investigation to reduce their noise content and to detrend it.

One of the alternative algorithms to the well-known Empirical Mode Decomposition (EMD) [34] for the decomposition of nonstationary and nonlinear signals is the basic Iterative Filtering (IF) algorithm initially introduced by Lin *et al.* in 2009 [35]. The properties and characteristics of this technique, also in comparison with the EMD, have been already extensively presented and discussed in previous works, e.g. [28, 36-40, 73-76]. The mathematical analysis of the IF method [36, 41-44, 70-72] allows both to guarantee a priori its convergence and to accelerate the algorithm via the Fast Fourier Transform producing the aforementioned FIF technique [41, 44].

The IF method has been extended in [45] to deal with 2D and higher dimensional signals. In this work, the FIF algorithm is extended, introducing the 2D Fast Iterative Filtering (FIF2) (Tab. S1 – see the 'Supplementary Material' section). A Matlab version of the proposed FIF2 algorithm is available at www.cicone.com.

FIF has been also extended to deal with multivariate signals, which are multichannel signals which are varying over time [46]. The proposed method, instead, considers signals which are varying over space, but not over time.

In FIF2 the input s is an image and the FFT and iFFT represent the 2D Fast Fourier Transform and inverse Fast Fourier Transform, respectively. As for the 1D version, the filter function w is chosen to be a positive, compactly supported bidimensional function with unitary volume, which has been convolved with itself to guarantee the convergence of the method [36, 45].

The authors point out that in Eq. 11 (see the 'Supplementary Material' section) the products as well as powers are all entry-wise. They are the so-called Hadamard products and powers. Working in the frequency domain still allows to check the classical stopping criterion for the IF scheme, thanks to the isometry property of the FFT.

In Figures 11 and 12, the authors show examples of a 2D thermal image pre-processing (PreP) by means of the proposed FIF2 algorithm compared with a Discrete Wavelet Transform (DWT) and Multidimensional Ensemble EMD (MEEMD) pre-processing [77,78]. The original thermal image is shown in the left panels of the first rows. The filtered mesh produced using DWT, MEEMD, and FIF2 are shown in the right panel of the first rows and the left and right panels of the second rows, respectively. To produce the MEEMD, an ensemble of 100 elements is considered, as suggested in the papers [77,78]. For the DWT, the Daubechies wavelet 'db45' were used.

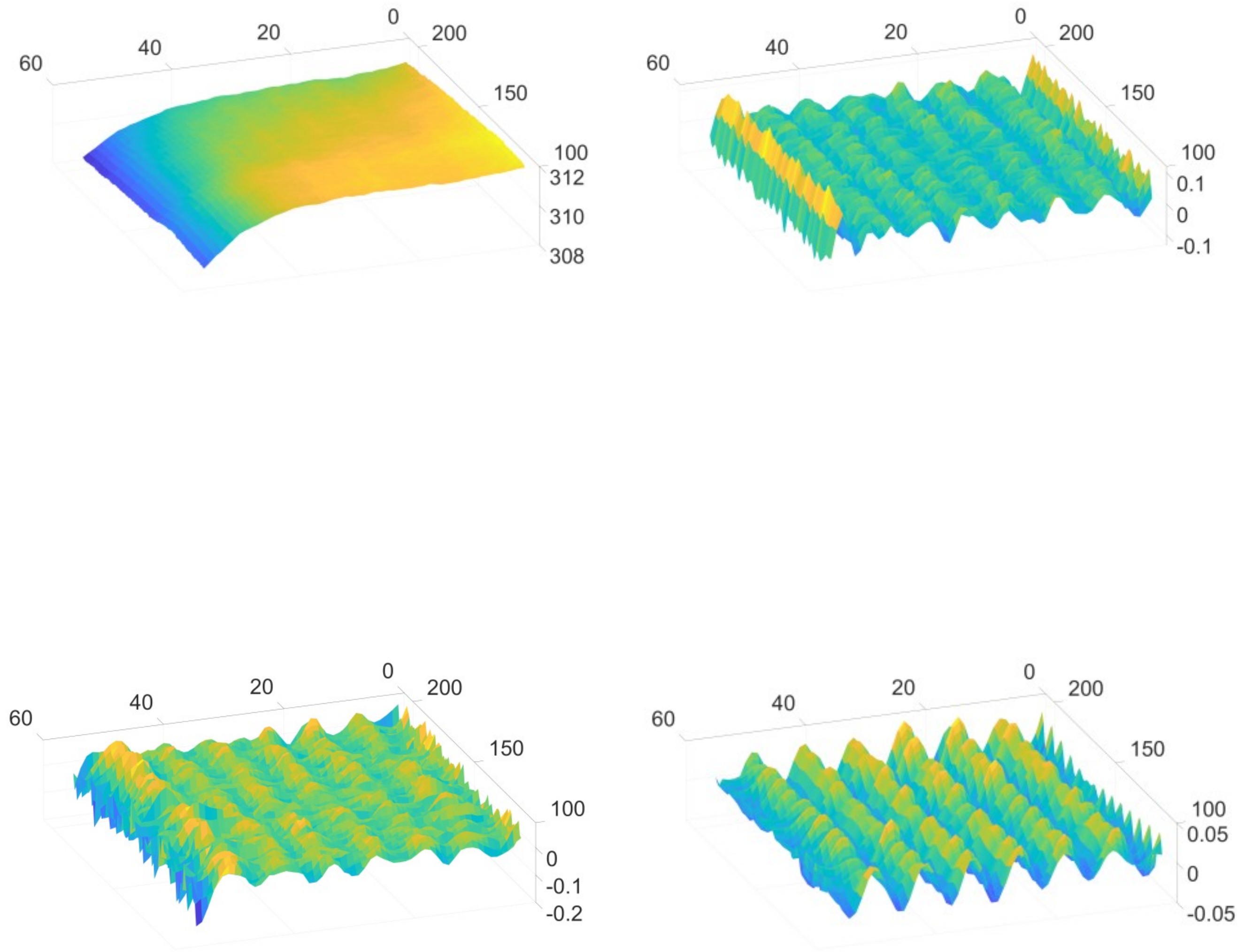

Fig. 11: First row: left panel, original thermal image of the grey area 2 of the specimen, ref. Fig. 1a. Right panel, after PreP using DWT. Second row: left panel, MEEMD PreP. Right panel, FIF2 PreP.

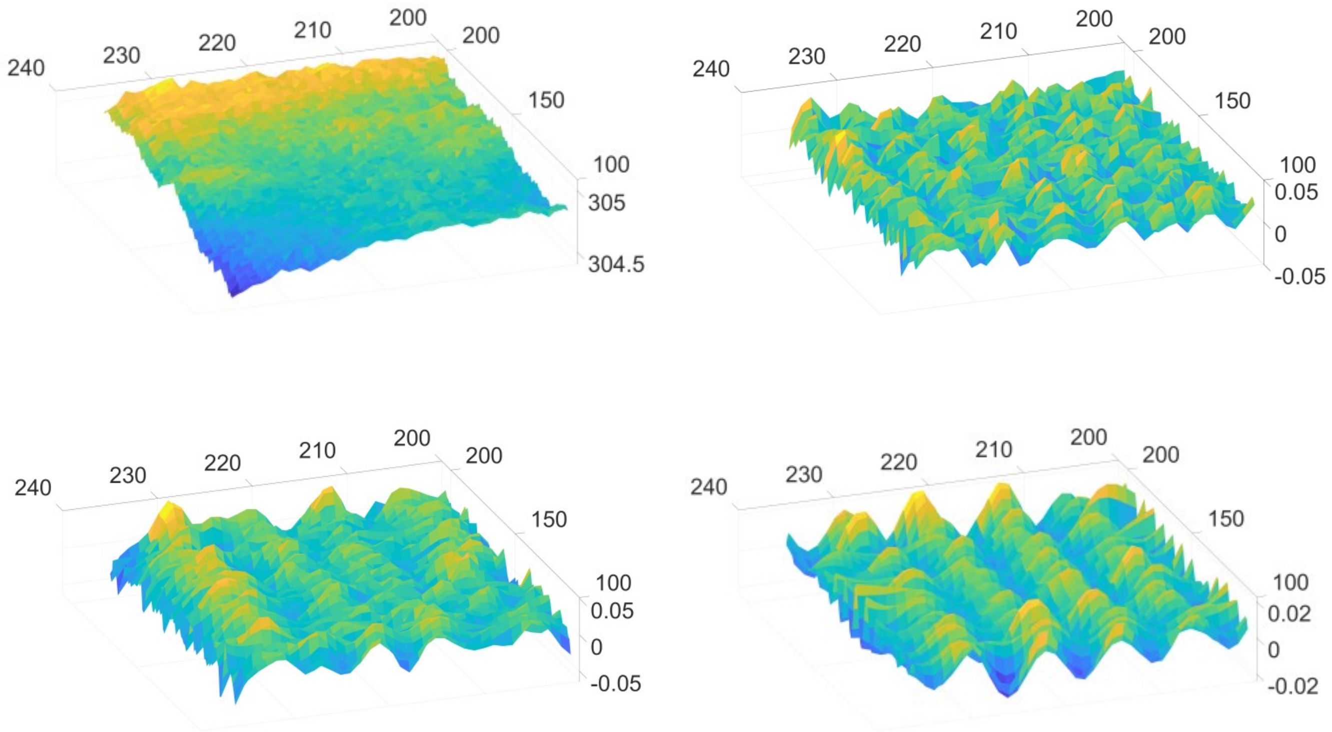

Fig. 12: First row: left panel, original signal, the yellow area 1 of the specimen, ref. Fig. 1a. Right panel, after PreP using DWT. Second row: left panel, MEEMD PreP. Right panel, FIF2 PreP.

The computational time of these three PreP techniques applied to a dataset containing 500 images is listed in Tab. 2. The algorithms were run on a PC (Intel(R) Core (TM) i7-8550U CPU, 1.80GHz, RAM 16.00GB, 64 bit Operating System) and the processing was conducted using MATLAB R2020a. The authors point out that, for the MEEMD, they opted for one of the smallest ensemble sizes. For the MEEMD the authors considered only one image out of 500 because the computational time was prohibitive. For one image, in fact, the MEEMD method required 1537 seconds to decompose the grey area 2 (Fig. 1a), which is a 55×101 pixels image, and 1304 seconds to decompose the yellow area 1 (Fig. 1a), which is instead a 36×101 pixels image. This means that MEEMD PreP of 500 images would cost more than 8 days of calculations for the grey area, and more than 7 days of calculations for the yellow one, if the ensemble of 100 elements per image is used. To make things even more difficult, with the MEEMD technique, in order to guarantee the proper stability of this method, it is usually advisable to use at least 200-800 elements for each ensemble, like for its 1D version of this algorithm, called EEMD [77,78].

Furthermore, considering that in the literature it has been extensively observed that FIF, EEMD, and their extensions which handle multidimensional and multivariate signals, produce comparable results [37,45,46,72], from now on the authors focus on the comparison of PreP performance of the DWT and FIF2 methods.

Table 2 – Computational time, in seconds, for the PreP of the 500 images corresponding to two areas of the specimen (i.e., area 1 in Fig. 1a and area 2 in Fig. 1a). The PreP has been done using MEEMD, DWT, and FIF2 techniques.

PreP time	MEEMD	DWT	FIF2
Grey area (area 2 – Fig. 1a)	1537×500	42 s	76 s
Yellow area (area 1 – Fig. 1a)	1304×500	37 s	59 s

6. Post-processing techniques

Once the data have been pre-processed using DWT and FIF2, the authors proceed to post-process (PostP) them using several approaches.

Principal component analysis (PCA) [46,48] in thermography (PCT) [49] given an important influence on post-analysis of thermal images, such as detection of defects for infrared non-destructive testing (IR-NDT) [50-54], art and archeological investigations [55,56], and it is also used for dimension reduction, noise elimination, classification, *etc*. PCT calculation can be performed by using covariance matrix calculation, singular value decomposition (SVD), which is used often in IR-NDT, or candid covariance-free incremental principal component thermography (CCIPCT) [56,58]. The decomposition process conducts using $X = U \Gamma V^T$ where X is a matrix with $\boldsymbol{p}\times\boldsymbol{n}$, dimension where $\boldsymbol{n}$ is the vectorized thermal image in every sequence and $\boldsymbol{p}$ corresponds to the number of observations, $\boldsymbol{p} > \boldsymbol{n}$ and Γ is a diagonal matrix with a dimension of $\boldsymbol{n}\times\boldsymbol{n}$ and either zero or positive elements. It is considered as the singular value of matrix $\boldsymbol{X}$ and V^T denotes the transpose of the $\boldsymbol{n}\times\boldsymbol{n}$ matrix (eigenvector or basis matrix) and $\boldsymbol{U}$ is the $\boldsymbol{p}\times\boldsymbol{n}$ matrix (n observations and p spatial variations). The columns of matrix $\boldsymbol{U}$ represent the input matrix (frame here) [49]. The basis matrix carries the orthonormal characteristic that also maximizes the variance of projected data, which leads to the principal components (PCs) of the input matrix (X) extracted from the basis V^T).

Another important observation regarding PCA based methods is that they cannot impose constraints for the non-negative basis of matrix X. Sparse non-negative matrix factorization (NMF) provided such constraint [67] and it is currently used in IR-NDT. The authors applied NMF using also two alternative approaches: gradient descent (GD), and non-negative least square (NNLS) [68-70].

These PostP methods enabled appropriate approximation selection among the component images. Furthermore, they allowed applying a threshold to separate the defects from the background and compare them to reference images.

6.1. Performance measurement procedure adopted in this study

To evaluate the performance of the combination of the different PreP and PostP methods applied to thermal images, the authors applied the following procedure.

First, to calculate the quantitative accuracy, the authors employed a binary image as ground truth (GT) as a reference for the calculation. The GTs were labeled the pixels in defects and background of the specimens by 0 intensity.

Then, the authors computed for each of the 10 images, produced by different PostP techniques of the PreP data, the area under the curve (AUC), based on the receiver operating characteristic (ROC) curve. The authors selected the image to be further analyzed the one corresponding to the maximal AUC value.

It is important to remind that the ROC curves are commonly used to quantify the performance of a classifier [79]. In particular, the ROC curve is plotted in a Cartesian plane where the vertical axis represents the ratio of the true positive to the total number of pixels that do correspond to the ground truth, called the true positive rate (Eq. 12), and on the horizontal axis the ratio of the false positive to the total number of pixels that do not contain the ground truth, called the false positive rate (Eq. 13). Both the true positive and false-positive rates are computed for different values of the threshold τ

$$true\ positive\ rate\left(TPr\right)=\frac{true\ positive}{actual\ ground\ truth\ pixels}$$

(12)

$$false\ positive\ rate\left(FPr\right)=\frac{false\ positive}{actual\ ground\ truth\ pixels}$$

(13)

The ROC curve is a non-decreasing curve that goes from (0, 0) to (1, 1) as the threshold τ varies. The classification produced using a random guess has a corresponding ROC curve which is the straight line connecting (0, 0) and (1, 1). The larger the area under the ROC curve (AUC), the better the performance of the classifier. For more details on ROC curves, the interested reader can refer to [79].

Subsequently, the authors computed the Precision, Recall, and Accuracy indices of the selected post-processed image, and computed, as the threshold, the one determining the maximal Accuracy value.

These three indices are defined as follows:

Precision = TP/(TP+FP)

Recall = TP / (TP+FN)

Accuracy = (TP+TN)/(TP+TN+FP+FN)

where TP stands for True Positive, FP for False Positive, TN for True Negative, and FN for False Negative.

Sometimes the maximum Accuracy value is achieved for the minimal or maximal value in the threshold range. In the present case, the authors opted for using a threshold value the one associated with the maximum of the Precision curve.

6.2. **Results and discussion of the experimental part**

The authors applied the previously described approach to the thermal images based on the main data presented in Sections 2 and 3. Figures 13, 14, and 15 present qualitative results of the grid detection using the state-of-the-art approaches of matrix decomposition algorithms. The qualitative results of CCIPCT,

PCT, NMF, NMF-gd, and NMF-nnls indicated significant accuracy to detect the grid inside the specimen using the PreP approach. Also, the results before PreP approaches (Fig. 13) indicates much lesser visibility of the grid structure in the infrared images and hence less highlighted in the results of the decomposition algorithms.

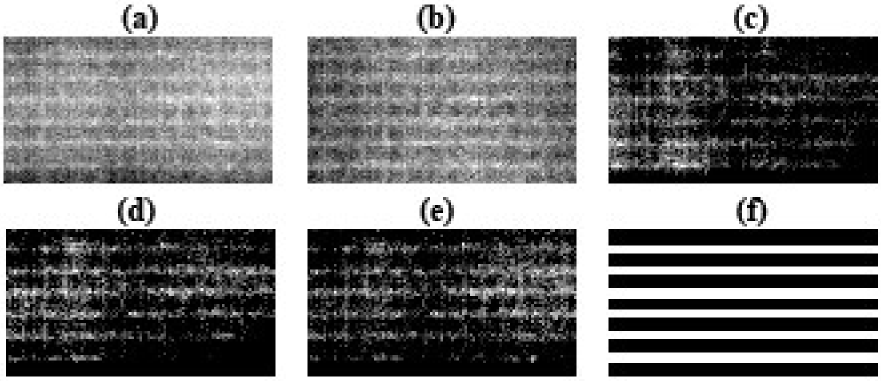

Fig. 13: The results of PostP applied to raw thermal data. CCIPCT (a), PCT (b), NMF (c), NMF-gd (d), and NMF-nnls (e) show the grid structure in the specimen, but each of them presents some noise. (f) represents the GT.

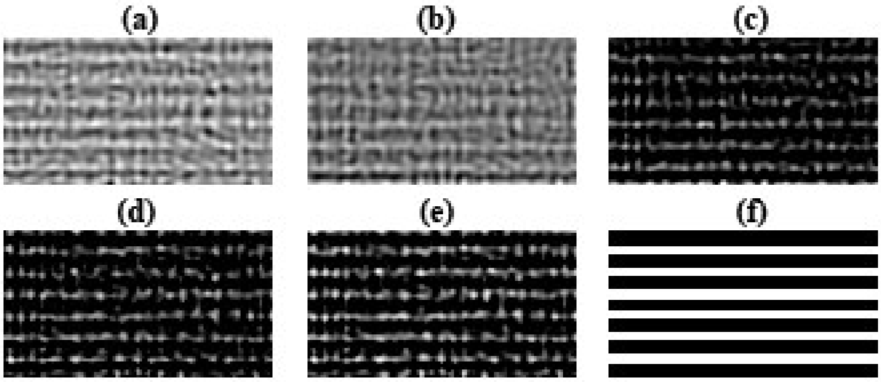

Fig. 14: The PostP results for DWT pre-processed thermal data. CCIPCT (a), NMF (c), NMF-gd (d), and NMF-nnls (e) show with significant accuracy the grid structure in the specimen. PCT (b) presents the lowest quality. (f) represents the GT.

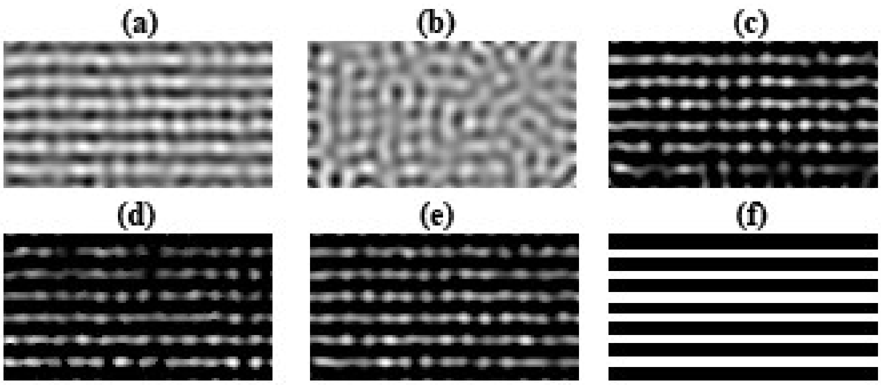

Fig. 15: The PostP results for FIF2 pre-processed thermal data. CCIPCT (a), NMF (c), NMF-gd (d), and NMF-nnls (e) show with good accuracy the grid structure in the specimen. PCT (b) in this case has clear problems. (f) represents the GT.

In Table 3, Precision, Recall, and Accuracy quantitative values are shown; they were evaluated for the grey area, one layer case (see area 2 of Fig. 1a), of the data without PreP, during the heating phase of the surface (i.e., the first 120 seconds of the test).

The performance inherent to DWT and FIF2 used as PreP is reported, instead, in Tables 4 and 5, respectively.

Table 3 – Performance of the PostP techniques when applied to the raw data for the grey area of the specimen (i.e., area 2 of Fig. 1a), one layer case, during the heating of the surface, first 120 seconds.

Method	Precision	Recall	Accuracy	Threshold based on
CCIPCT	0.66314	0.43465	0.71413	Acc
NMF	0.62548	0.48614	0.70729	Acc
PCT	0.72547	0.36238	0.71827	Acc
NMF-gd	0.71983	0.41337	0.72817	Acc
NMF-nnls	0.64773	0.53069	0.72439	Acc

Table 4 – Performance of the PostP techniques when applied to the DWT pre-processed data for the grey area of the specimen (i.e., area 2 of Fig. 1a), one layer case, during the heating of the surface, first 120 seconds.

Method	Precision	Recall	Accuracy	Threshold based on
CCIPCT	0.69574	0.69505	0.77858	Acc
NMF	0.70445	0.65842	0.77534	Acc
PCT	0.65471	0.5604	0.73267	Acc
NMF-gd	0.68357	0.66733	0.7667	Acc
NMF-nnls	0.71387	0.72871	0.79514	Acc

Table 5 – Performance of the PostP techniques when applied to the FIF2 pre-processed data for the grey area of the specimen (i.e., area 2 of Fig. 1a), one layer case, during the heating of the surface, first 120 seconds.

Method	Precision	Recall	Accuracy	Threshold based on
CCIPCT	0.85742	0.87525	0.90171	Acc
NMF	0.82969	0.80792	0.86985	Acc
PCT	0.53386	0.13267	0.64248	Acc
NMF-gd	0.86603	0.80644	0.88425	Acc
NMF-nnls	0.83387	0.8896	0.89541	Acc

From the comparison of the performance values of the different PostP techniques applied to the raw thermal data (see Fig. 13 and Tab. 3) with the ones obtained after PreP the data with DWT and FIF2 methods (see Figs. 14, 15, and Tabs. 5, 6, respectively), it is evident that the performance after FIF2 PreP is always better than the other cases. The only exception is when PCT is used for PostP the data. In this case, the DWT proves to be better than FIF2 for PreP. This is true for the heating stage (first 120 seconds) of the grey area (i.e., area 2 in Fig. 1a).

Similar results are obtained during the cooling phase of the data (i.e., the last 380 seconds) and for the heating and cooling time window of the yellow area (i.e., the scattered hemp fibres layer – see area 1 in Fig. 1a), where the specimen has two layers of material covering the reinforcing grid. In these last three cases, the FIF2 PreP approach allowed to outperform the results obtained with raw and DWT pre-processed data for all PostP methods, even the PCT algorithm.

The corresponding Tables (i.e., Tables S2-S10), that contain the quantitative results, are reported in the supplementary material of this manuscript.

7. Validation of the numerical analysis for a specific material via the Parker method

The characterization of the thermal diffusivity of the coating layer (i.e., the most important part of the specimen: see the area called **1** in Fig. 1a) follows the in-depth study previously described, which validates our analyses. The interest was focused on a local behavior and, fortunately, the thickness of the layer made by scattered hemp fibres is both very thin (Tab. 1) and exposed to air (Fig. 16). An extremely dense swept mesh was used to ensure that the diffusivity calculation was effectively linked to a discretization having stratified nodal elements. The stratification took place onto defined levels, which started from the front face and ended on the rear face of the specimen. The authors verified that the Biot number was within the range (0-1). This verification formally allowed to treat the surface layer as a coating and, therefore, calculating its diffusivity via the Parker method. Concerning this method, the duration of the pulse was adjusted from a few seconds to several seconds to achieve the desired temperature rise depending on both the thickness of the material and its thermal properties.

In Eq. 14, the Biot number is shown.

$$Bi = \frac{h \cdot L}{\lambda} \tag{14}$$

where h is the convective coefficient expressed in W/m^2K, L is the thickness of the layer under analysis in [m], and λ is the thermal conductivity in W/mK. A value of Bi = 0.5263157 was obtained allowing us to use the Parker method. By considering the low value found, the vacuum bell with reflecting walls (that is able to reduce both the exchanging heat by convection and radiation) was not used.

The thermal diffusivity can be interpreted as a measure of thermal inertia (e.g., heat propagates slowly where the thermal diffusivity is low). The components of the thermal diffusivity α, when given on tensor form (i.e., α_{xx}, α_{yy}, and so on, representing an anisotropic thermal diffusivity), are available as specific Comsol® functions. The single scalar mean thermal diffusivity is the mean value of the diagonal elements α_{xx}, α_{yy}, and α_{zz} [80].

It should be noted that for isotropic materials, the diffusivity value may be calculated through the single scalar diagonal elements according to the well-known Eq. 15.

$$\alpha = \frac{\lambda}{\rho c_p} = \frac{0.038}{25 \cdot 1700} = 8.94 \cdot 10^{-7} \frac{m^2}{s} \tag{15}$$

In our case, the material is anisotropic. Therefore, it is not correct to calculate α via Eq. 15. For this reason, the Parker equation suitable for the calculation of α also for anisotropic materials is reported as Eq. 16.

$$\alpha = \frac{0.139 \cdot L^2}{t_{0.5}} \tag{16}$$

where, L^2 is the thickness of the scattered hemp fibres layer in [cm], and $t_{0.5}$ represents the time necessary for the thermal load imposed by a laser source on the layer **1** (Fig. 1a) to propagate for a specific value of the normalized temperature, T_n. Particular attention was paid to the term $t_{0.5}$ expressed in [s]. In fact, $t_{0.5}$ corresponds to the time in [s] when T_n is equal to 0.5. Obviously, the trend of T_n was calculated only for the scattered hemp fibres layer. In this regard, by adding a Comsol® virtual probe on the scattered hemp fibres layer (see, for reference, Fig. 16), the temperature evolution in the form of heat was analyzed for its entire thickness. The experimental test involved the use of a laser working into 445–450 nm (blue color) that thermally charged a specific part of the specimen according to the setup shown in Fig. 16.

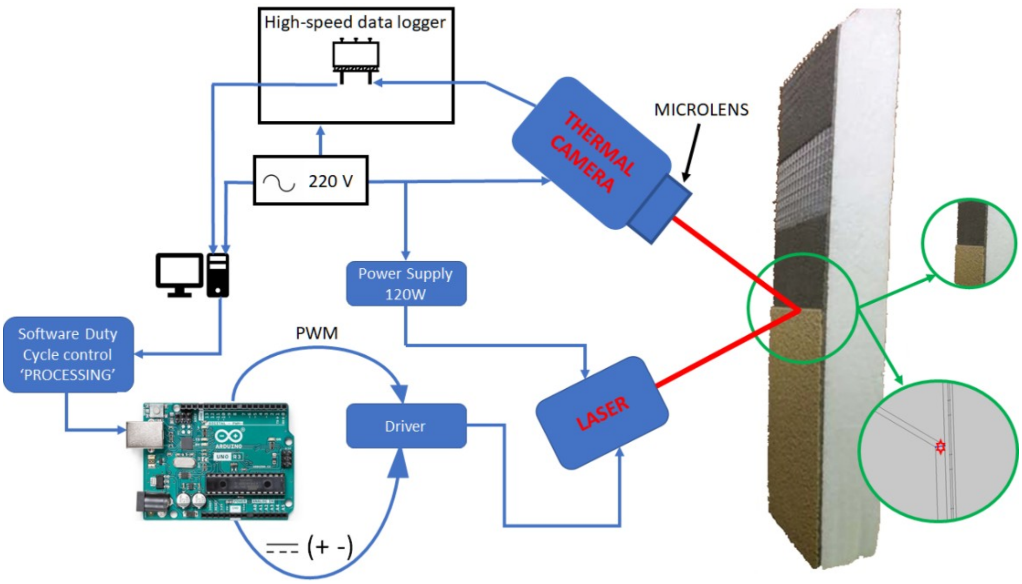

Fig. 16: Experimental setup for the evaluation of the thermal diffusivity of the scattered hemp fibres layer (area 1, Fig. 1a); PWM = pulse-width modulation. The red asterisk on the panel indicates the position of the Comsol® virtual probe.

In order to correctly replicate the experimental test in the numerical one, the laser power was set as a heat point load equal to 0.5 W by leaving this source to act for several seconds. The temperature was normalized in the numerical model obtaining the trend shown in Fig. 17.

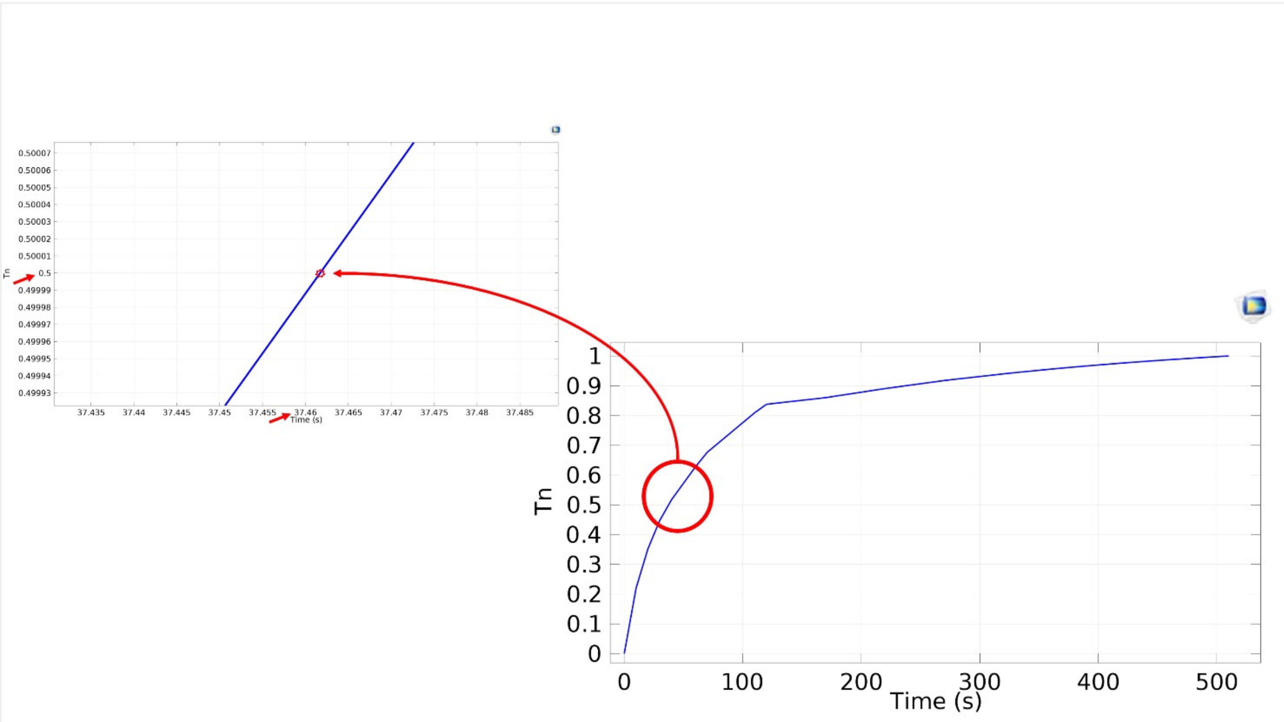

Fig. 17: Time course of the normalized temperature calculated for the scattered hemp fibres layer only. The magnification in the figure helps the reader to identify the instant of time $t_{0.5}$ necessary for the calculation of α.

Since the numerical model is especially designed for this calculation, it can be assumed that the value of α (calculated starting from $t_{0.5}$ – see the red arrow added along the *y-axis* of Fig. 17) is actually adiabatic. Therefore, by completing Eq. 16 with the time value $t_{0.5}$ shown in Fig. 17, the following value of α is obtained (Eq. 17).

$$\alpha = \frac{0.139 \cdot 0.1^2}{37.46} = 0.0000371 \left[\frac{cm^2}{s} \right] \quad (17)$$

Following the test whose layout is shown in Fig. 16, the normalized curve of the T_n trend was obtained from the thermographic test. Fig. 18 shows both the numerical and experimental trends. In this way, the reader is able to estimate the two different trends. In addition, it also allows to understand the percentage error existing between the theoretical trend (blue dotted line) and the experimental one (red solid line).

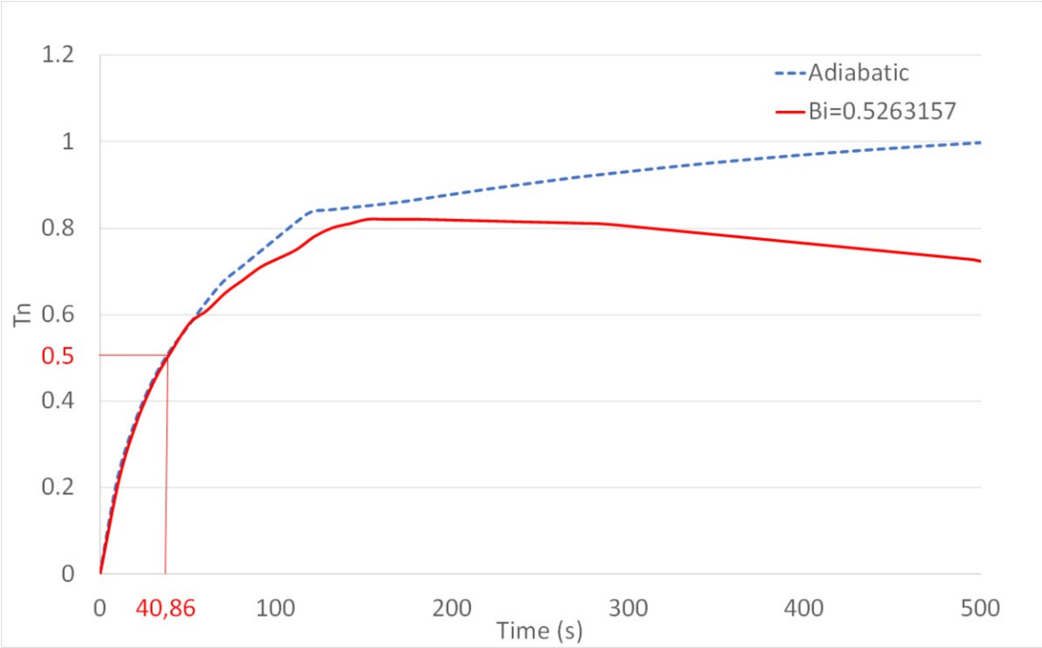

Fig. 18: Time course of the normalized temperature. Adiabatic (dashed blue): numerical test; Bi = 0.5263157 (dashed red): thermographic test.

Finally, the value of α for the experimental test was calculated by Eq. 18.

$$\alpha = \frac{0.139 \cdot 0.1^2}{40.86} = 0.0000340207 \left[\frac{cm^2}{s} \right] \tag{18}$$

The difference between the data reported in Eqs. 17 and 18 show that the experimental value of α is ~8.3% lower than the modeled one, and that the response times of the thermal load on the surface opposite to the heated one were 37.46 s (see the red arrow added along the *x-axis* of Fig. 17) for the numerical case and 40.86 s (see the *x-axis* of Fig. 18) for the experimental one.

8. Conclusions

The numerical model, albeit with a high computational cost, highlighted the opportunity to work without the use of a high performance computing device, thanks to the use of the work plane procedure. This technique allowed to conduct the whole processing on a personal computer, showing the results of the model both for the temperature field in the volumetric form and along the lines set for the directions of interest. In particular, through volumetric graphics, it is possible to understand the spatial temperature field that the model undergoes in its temporal evolution for each point in space. On the other hand, the use of the directrices helps the reader to follow the evolution of the temperature field within the model itself. This idea is useful to understand the mutual interactions between different materials in the contact areas, that followed an advanced mechanical treatment [81]. Finally, the model showed the presence of a phase shift, typical of thermal insulation materials, also for the layers made with mortars. This can certainly be attributed to the styrofoam support, which is known to have excellent thermo-insulating properties, but also to the layer of hemp fibres. The latter has shown good thermal-insulating characteristics albeit with only a thin layer applied as an external coating. This initial result was confirmed by applying advanced algorithms to thermographic (experimental) data [82–85].

In fact, in this work, a new 2D fast algorithm for the thermal data pre-processing is developed, called 2D Fast Iterative Filtering (FIF2), and its pseudo-code is presented. This newly developed algorithm proves to be extremely faster than previously developed methods, like the MEEMD, and to be comparable, from a computational time perspective to the DWT technique.

Subsequently, pre-processed thermal images have been post-processed using several methods available in the literature. In particular, the authors considered the CCIPCT, PCT, NMF, NMF-gd, and NMF-nnls methods, to identify the grid localization inside the specimen. For each post-processing algorithm, ten images have been produced, and the one corresponding to the maximal area under the curve (AUC) value, based on the receiver operating characteristic (ROC) curve, has been selected. Then, the performance of the different post-processing techniques has been studied and compared using Precision, Recall, and Accuracy metrics.

From these results, it becomes evident that all thermal images post-processing approaches increase their performance when FIF2 pre-processing is applied, versus the DWT pre-processing, or versus using raw thermal images. The only exception is for PCT post-processing of the data in the heating phase of the grey area of the specimen (one layer case). In that case, the DWT pre-processed data produce better performance than FIF2 pre-processed ones. Nevertheless, during the cooling phase of the grey area 2, as well as for the heating and cooling time window of the yellow area 1 (i.e., the hemp fibres layer), where the specimen has two layers of material covering the reinforcing grid, the FIF2 pre-processing approach allowed to outperform the results obtained with raw and DWT pre-processed data for all post-processing methods, even the PCT algorithm.

Finally, the good agreement among the numerical test and the thermographic one was verified by applying the Parker method on the most important part of the specimen (i.e., the scattered hemp fibres layer), by finding a low Biot number that allowed simplifications in the experimental setup.

Acknowledgments

A. Cicone and L. Robol are member of the Italian “Gruppo Nazionale di Calcolo Scientifico” (GNCS) of the Istituto Nazionale di Alta Matematica "Francesco Severi" (INdAM). A. Cicone work was partially supported through the CSES-Limadou project of the Istituto di Astrofisica e Planetologia Spaziali (IAPS) of the Istituto Nazionale di Astrofisica (INAF).

The authors would like to thank Eng. Massimo Cretarola who helped to build part of the experimental setup shown in Fig. 16.

References

[1] Seed, L., Houghton, A., Heron, A., Hobson, G.S., Powell, A.R., Tozer, R.C.: 'Real time processing of infrared images from road traffic'. In: Proceedings of SPIE – The International Society for Optical Engineering, **590**, 1986, p. 233–240.

[2] Cremer, F., De Jong, W., Schutte, K.: 'Processing of polarimetric infrared images for landmine detection'. In: Proceedings of the 2nd International Workshop on Advanced Ground Penetrating Radar, 2003, p. 216–221.

[3] Rainieri, S., Bozzoli, F., Pagliarini, G.: 'Wiener filtering technique applied to thermographic data reduction intended for the estimation of plate fins performance', Experimental Thermal and Fluid Science, **28**, 2004, pp. 179–183.

[4] Vardasca, R., Bajwa, U.: 'Segmentation and noise removal on thermographic images of hands', Thermology International, **18**, 2008, pp. 89–94.

[5] San Martín, C., Meza, P., Torres, S., Carrillo, R.: 'Improved infrared face identification performance using nonuniformity correction techniques', Lectures Notes in Computer Science (including subseries Lecture Notes

in Artificial Intelligence and Lecture Notes in Bioinformatics), **5259**, 2008, pp. 1115–1123.

[6] Liu, Z.-Y., Zhou, F.-G., Bai, X.-Z.: 'Target location for IR image based on IR/visual image registration'. In: Proceedings of SPIE – The International Society for Optical Engineering, **7383**, 2009, article number 738336.

[7] Liu, Z., Jiang, Y., Lv, J., Zhu, H.: 'Adaptive NUC algorithm for uncooled IRFPA based on neural networks'. In: Proceedings of SPIE – The International Society for Optical Engineering, 5th International Symposium on Advanced Optical Manufacturing and Testing Technologies: Optoelectronic Materials and Devices for Detector, Imager, Display, and Energy Conversion Technology, Dalian (China) **7658**, 2010, article number: 76582W.

[8] Hidalgo-Gato, R., Mingo, P., López-Higuera, J.M., Madruga, F.J.: 'Pre-processing techniques of thermal sequences applied to online welding monitoring', Quantitative InfraRed Thermography Journal, **9**, 2012, pp. 69–78.

[9] Peng, Z., Wang, X., Lu, J.: 'A heating window effect imaging experiment and its analysis'. In: Proceedings of SPIE – The International Society for Optical Engineering, 5th International Symposium on Photoelectronic Detection and Imaging (ISPDI), Beijing (China) **8907**, 2013, article number: 890715.

[10] Wang, P., Gao, L., Chen, G.-Q., Ding, R.-J.: 'Design of real-time image processing system for IRFPA based on FPGA'. In: Proceedings of SPIE – The International Society for Optical Engineering, 5th International Symposium on Photoelectronic Detection and Imaging (ISPDI), Beijing (China) **8907**, 2013, article number: 89071B.

[11] Murariu, A.C., Crasteti, S.: 'Nondestructive assessment of anticorrosive aluminium coatings by active infrared thermography', Advanced Materials Research, **814**, 2013, pp. 235–243.

[12] Hidalgo-Gato, R., González De Ulloa, L., Andrés, J.R., Martínez, S., Pérez, A., Madruga, F.J., López-Higuera, J.M.: 'A thermographic step-heating technique for metallic pollutant detection in soils', Infrared Physics and Technology, **69**, 2015, pp. 191–197.

[13] Halloua, H., Elhassnaoui, A., Saifi, A., Elamiri, A., Obbadi, A., Errami, Y., Sahnoun, S.: 'Neural networks and genetic algorithms for the evaluation of coatings thicknesses in thermal barriers by infrared thermography data', Procedia Structural Integrity, **5**, 2017, pp. 997–1004.

[14] Li, X., Gao, B., Woo, W.L., Tian, G.Y., Qiu, X., Gu, L.: 'Quantitative surface crack evaluation based on eddy current pulsed thermography', IEEE Sensors Journal, **17**, 2017, pp. 412–421.

[15] Kurpinski, M., Fidali, M.: 'Improvement of bonded joint defects visibility by use of selected infrared image processing methods', Applied Condition Monitoring, **10**, 2018, pp. 169–180.

[16] Zhang, H., Avdelidis, N.P., Osman, A., Ibarra-Castanedo, C., Sfarra, S., Fernandes, H., Matikas, T.E., Maldague, X.P.V.: 'Enhanced infrared image processing for impacted carbon/glass fiber-reinforced composite evaluation', Sensors, **18**, 2018, article number: 45.

[17] Moustakidis, S., Anagnostis, A., Chondronasios, A., Karlsson, P., Hrissagis, K.: 'Excitation-invariant pre-processing of thermographic data', Proceedings of the Institution of Mechanical Engineers, Part O: Journal of Risk and Reliability, **232**, 2018, pp. 435–446.

[18] Shanmugan, C., Chandira Sekaran, E.: 'IRT image segmentation and enhancement using FCM-MALO approach', Infrared Physics and Technology, **97**, 2019, pp. 187–196.

[19] Wang, D., Wang, Z., Zhu, J., Ciampa, F.: 'Enhanced pre-processing of thermal data in long pulse thermography using the Levenberg-Marquardt algorithm', Infrared Physics and Technology, **99**, 2019, pp. 158–166.

[20] Wang, Q., Hu, Q., Qiu, J., Pei, C., Li, X., Zhou, H., Xia, R., Liu, J.: 'Image enhancement method for laser infrared thermography defect detection in aviation composites', Optical Engineering, **58**, 2019, article number: 103104.

[21] Kaur, K., Mulaveesala, R.: 'An efficient data processing approach for frequency modulated thermal wave imaging for inspection of streel material', Infrared Physics and Technology, **103**, 2019, article number: 103083.

[22] Maskuri, N.L., Abu Bakar, M.H., Ismail, A.K.: 'The image processing technique of defect detection in metal materials using active infrared thermography', Advanced Structured Materials, **131**, 2020, pp. 151–160.

[23] Barreira, E., Almeida, R.M.S.F., Simões, M.L., Rebelo, D.: 'Quantitative infrared thermography to evaluate the humidification of lightweight concrete', Sensors, **20**, 2020, article number: 1664.

[24] Ratsakou, A., Reboud, C., Skarlatos, A., Lesselier, D.: 'Model based characterisation of delamination by means of thermographic inspection', Journal of Phsics: Conference Series, **1476**, 2020, article number: 012005.

[25] Díaz, J.J.L., Vlaminck, M., Lefkaditis, D., Vargas, S.A.O., Luong, H.: 'Solar panel detection within complex backgrounds using thermal images acquired by uavs', Sensors, **20**, 2020, pp. 1–16.

[26] Castellini, P., Martarelli, M., D'Antuono, A., Paone, N.: 'Soft-sensing reconstruction of in-depth defect geometry fron active IR-thermography data', Measurement Science and Technology, **31**, 2020, article number: 125902.

[27] Hu, J., Zhang, H., Sfarra, S., Sergi, C., Perilli, S., Ibarra-Castanedo, C., Tian, G., Maldague, X.: 'Enhanced infrared sparse pattern extraction and usage for impact evaluation of basalt-carbon hybrid composites by pulsed thermography', Sensors, **20**, 2020, pp. 1–18.

[28] Sfarra, S., Cicone, A., Yousefi, B., Ibarra-Castanedo, C., Perilli, S., Maldague, X.: 'Improving the detection of thermal bridges in buildings via on-site infrared thermography: the potentialities of innovative mathematical tools', Energy & Buildings, **128**, 2019, pp. 159–171.

[29] Perilli, S., Regi, M., Sfarra, S., Nardi, I.: 'Comparative analysis of heat transfer for an advanced composite material used as insulation in the building field by means of Comsol Multiphysics® and Matlab® computer programs', Romanian Journal of Materials, **46**, 2016, pp. 185–195.

[30] Liu, K., Perilli, S., Chulkov, A.O., Yao, Y., Omar, M., Vavilov, V., Liu, Y., Sfarra, S.: 'Defining the thermal features of sub-surface reinforcing fibres in non-polluting thermo-acoustic insulating panels: a numerical-thermographic-segmentation approach', Infrastructures, **6**, 2021, pp. 1–30.

[31] Parker, W.J., Jenkins, R.J., Butter, C.P., Abbot, G.L.: 'Flash method of determining thermal diffusivity, heat capacity and thermal conductivity', J. Appl. Phys, **32**, 1961, pp. 1679–1684.

[32] Data sheet of the OSRAM lamps. http://www.osram.com/media/resource/hires/333561/theratherm_siccatherm_infrared-en.pdf. Accessed 04 January 2021.

[33] Comsol. https://www.comsol.com/blogs/much-memory-needed-solve-large-comsol-models/. Accessed 04 January 2021.

[34] Huang, N.E., Shen, Z.,Long, S.R., Wu, M.C., Shih, H.H., Zheng, Q.,Yen, N.C., Tung, C.C., Liu, H.H.: 'The empirical mode decomposition and the Hilbert spectrum for nonlinear and non-stationary time series analysis'. Proceedings of the Royal Society of London. Series A: Mathematical, Physical and Engineering Sciences, **454**, 1998, pp. 903.

[35] Lin, L., Wang, Y., Zhou, H.: 'Iterative filtering as an alternative algorithm for empirical mode decomposition',

Adv. Adapt. Data Anal., **1**, 2009, pp. 543–560.

[36] Cicone, A., Liu, J., Zhou, H.: 'Adaptive local iterative filtering for signal decomposition and instantaneous frequency analysis', Appl. Comput. Harmon. Anal., **41**, 2016, pp. 384–411.

[37] Cicone, A.: 'Nonstationary signal decomposition for dummies', Advances in Mathematical Methods and High Performance Computing, Advances in Mechanics and Mathematics 41, Chapter 3, Springer Nature, 2019.

[38] Piersanti, M. , Materassi, M. , Cicone, A. , Spogli, L., Zhou, H., Ezquer, R. G.: 'Adaptive Local Iterative Filtering: a promising technique for the analysis of non-stationary signals'. Journal of Geophysical Research - Space Physics, 123 (1), 2018, pp. 1031-1046.

[39] Cicone, A., Liu, J., Zhou, H.: 'Hyperspectral chemical plume detection algorithms based on multidimensional iterative filtering decomposition', Phil. Trans. R. Soc. A: Math. Phys. Eng. Sci., **374**, 2016, pp. 20150196.

[40] Spogli, L., Piersanti, M., Cesaroni, C., Materassi, M., Cicone, A., Alfonsi, L., Romano, V., Ezquer, R.G.: 'Role of the external drivers in the occurrence of low-latitude ionospheric scintillation revealed by multi-scale analysis'. Journal of Space Weather and Space Climate, 9 (4), 2019, A35.

[41] Cicone, A., Zhou, H.: 'Numerical Analysis for Iterative Filtering with New Efficient Implementations Based on FFT', Numerische Mathematik 147, 2021, pp.1-28.

[42] Cicone, A., Dell'Acqua, P.: 'Study of boundary conditions in the Iterative Filtering method for the decomposition of nonstationary signals'. Journal of Computational and Applied Mathematics, 373, 2019, 112248.

[43] Cicone, A., Garoni, C., S. Serra-Capizzano, S.: 'Spectral and convergence analysis of the Discrete ALIF method'. Linear Algebra and its Applications, 580, 2019, pp. 62-95.

[44] Cicone, A.: 'Iterative Filtering as a direct method for the decomposition of non-stationary signals'. Numerical Algorithms, 85 (3) , 2020, pp. 811-827.

[45] Cicone, A., Zhou, H.: 'Multidimensional iterative filtering method for the decomposition of high-dimensional non-stationary signals', Numer. Math. Theory Methods Appl., **10**, 2017, pp. 278–298.

[46] Cicone, A., Pellegrino, E.: 'Multivariate Fast Iterative Filtering for the decomposition of nonstationary signals'. Submitted

[47] Pearson, K.: 'On Lines and Planes of Closest Fit to Systems of Points in Space' (PDF). Philosophical Magazine, **2**(11), 1901, pp. 559–572.

[48] Hotelling, H.: 'Analysis of a complex of statistical variables into principal components'. Journal of Educational Psychology, **24**, 1933, pp. 417–441, and pp. 498–520.

[49] Rajic, N.: 'Principal component thermography for flaw contrast enhancement and flaw depth characterization in composite structures', Composite Structures, **58**, 2002,pp. 521–528.

[50] H. Zhang *et al.*: 'Optical and Mechanical Excitation Thermography for Impact Response in Basalt-Carbon Hybrid Fiber-Reinforced Composite Laminates', IEEE Transactions on Industrial Informatics, **14**(2), 2018, pp. 514–522.

[51] H. Zhang *et al.*: 'Optical excitation thermography for twill/plain weaves and stitched fabric dry carbon fiber preform inspection', Composites Part A: Applied Science and Manufacturing, **107**, 2018, pp. 282-293.

[52] Fernandes, H., Zhang, H., Figueiredo, A., Malheiros, F., Ignacio, L. H., Sfarra, S., Ibarra-Castanedo, C., Guimaraes, G., Maldague, X.: 'Machine Learning and Infrared Thermography for Fiber Orientation Assessment on Randomly-Oriented Strands Parts', Sensors, **18**(1), 2018, 288.

[53] Ahi, K.: 'Mathematical modeling of THz point spread function and simulation of THz imaging systems', IEEE Transactions on Terahertz Science and Technology, **7**(6), 2017,pp. 747–754.

[54] Yousefi, B., Sharifipour, H.M., Ibarra-Castanedo, C., Maldague, X.P.: 'Automatic IRNDT inspection applying sparse PCA-based clustering'. In: Electrical and Computer Engineering (CCECE), 2017 IEEE 30th Canadian Conference on (pp. 1-4), 2017.

[55] Yousefi, B., Sfarra, S., Maldague, X.P.: 'Quantitative assessment in thermal image segmentation for artistic objects'. Optics for Arts, Architecture, and Archaeology VI, 10331, 2017, 1033108.

[56] Sfarra, S., Ibarra-Castanedo, C., Paoletti, D., Maldague, X.: 'Infrared vision inspection of cultural heritage objects from the city of L'Aquila, Italy and its surroundings', Materials Evaluation, **71**(5), 2013, pp. 561–570.

[57] Yousefi, B., Sfarra, S., Ibarra-Castanedo, C., Maldague, X.P.: 'Comparative analysis on thermal non-destructive testing imagery applying Candid Covariance-Free Incremental Principal Component Thermography (CCIPCT)', Infrared Physics & Technology, **85**, 2017, pp. 163–169.

[58] Yousefi, B., Sfarra, S., Ibarra-Castanedo, C., Maldague, X.P.: 'Thermal ndt applying candid covariance-free incremental principal component thermography (ccipct)'. In: Thermosense: Thermal Infrared Applications XXXIX, 10214, 2017, p. 102141I.

[59] Tillmann, A.M., Pfetsch, M.E.: 'The computational complexity of the restricted isometry property, the nullspace property, and related concepts in compressed sensing', IEEE Transactions on Information Theory, **60**(2), 2014, pp. 1248–1259.

[60] Tibshirani, R.: 'Regression shrinkage and selection via the lasso', Journal of the Royal Statistical Society. Series B (Methodological), 1996, pp. 267–288.

[61] Tibshirani, R.: 'The lasso method for variable selection in the cox model', Statistics in Medicine, **16**(4), 1997, pp. 385–395.

[62] Zou, H., Hastie, T.: 'Regularization and variable selection via the elastic net', Journal of the Royal Statistical Society: Series B (Statistical Methodology), **67**(2), 2005, pp. 301–320.

[63] Zou, H., Hastie, T., Tibshirani, R.: 'Sparse principal component analysis', Journal of Computational and graphical statistics, **15**(2), 2006, pp. 265–286.

[64] Yousefi, B., Sfarra, S., Sarasini, F., & Maldague, X. P.: 'IRNDT Inspection via Sparse Principal Component Thermography'. In 2018 IEEE Canadian Conference on Electrical & Computer Engineering (CCECE) (pp. 1-4). IEEE, 2018.

[65] Yousefi, B., Sfarra, S., Sarasini, F., Castanedo, C. I., & Maldague, X. P.: 'Low-rank sparse principal component thermography (sparse-pct): Comparative assessment on detection of subsurface defects'. Infrared Physics & Technology, **98**, 2019, pp. 278-284.

[66] Lee, D. D., & Seung, H. S.: 'Algorithms for non-negative matrix factorization'. In *Advances in neural information processing systems,* 2001, pp. 556-562.

[67] Kim, H., & Park, H.: 'Sparse non-negative matrix factorizations via alternating non-negativity-constrained least squares for microarray data analysis'. Bioinformatics, **23**(12), 2007, pp. 1495-1502.

[68] Yousefi, B., Sfarra, S., Ibarra-Castanedo, C., Avdelidis, N. P., & Maldague, X. P.: 'Thermography data fusion and nonnegative matrix factorization for the evaluation of cultural heritage objects and buildings'. Journal of

Thermal Analysis and Calorimetry, **136**(2), 2019, 943-955.

[69] Yousefi, B., Ibarra-Castanedo, C., & Maldague, X. P.: 'Infrared Non-Destructive Testing via Semi-Nonnegative Matrix Factorization'. In *Multidisciplinary Digital Publishing Institute Proceedings,* **27**(1), 2019, pp. 13.

[70] Cicone, A., Barbarino, G.: 'Conjectures on spectral properties of ALIF algorithm'. Submitted

[71] Cicone, A., Wu, H.-T.: 'Convergence analysis of Adaptive Locally Iterative Filtering and SIFT method'. Submitted

[72] Stallone, A., Cicone, A., Materassi, M.: 'New insights and best practices for the successful use of Empirical Mode Decomposition, Iterative Filtering and derived algorithms'. Scientific Reports, **10**(1), 2020, 15161.

[73] Materassi, M., Piersanti, M., Consolini, G., Diego, P., D'angelo, G., Bertello, I., Cicone, A.: 'Stepping into the equatorward boundary of the auroral oval: Preliminary results of multi scale statistical analysis'. Annals of Geophysics, **61**, 2018.

[74] Piersanti, G., Piersanti, M., Cicone, A., Canofari, P., Di Domizio, M.: 'An inquiry into the structure and dynamics of crude oil price using the fast iterative filtering algorithm', Energy Economics, **92**, 2020, 104952

[75] Spogli, L., Piersanti, M., Cesaroni, C., Materassi, M., Cicone, A., Alfonsi, L., Romano, V., Ezquer, R.G.: 'Role of the external drivers in the occurrence of low-latitude ionospheric scintillation revealed by multi-scale analysis', 2019 URSI Asia-Pacific Radio Science Conference, AP-RASC 2019, 2019, 8738254

[76] Ghobadi, H., Spogli, L., Alfonsi, L., Cesaroni, C., Cicone, A., Linty, N., Romano, V., Cafaro, M.: 'Disentangling ionospheric refraction and diffraction effects in GNSS raw phase through fast iterative filtering technique', GPS Solution*s*, **24**(3), 2020, 85.

[77] Wu, Z., Huang, N. E., Chen, X.: 'The Multi-Dimensional Ensemble Empirical Mode Decomposition Method', Advances in Adaptive Data Analysis, **1**(3), 2009, pp. 339–372.

[78] Wu, Z., Huang, N.E.: 'Ensemble empirical mode decomposition: A noise-assisted data analysis method', Advances in Adaptive Data Analysis, **1**, 2009, pp. 1–41.

[79] Fawcett T. 'An introduction to ROC analysis'. Pattern Recogn. Lett., **27**, 2006, pp. 861–874.

[80] https://doc.comsol.com/5.4/doc/com.comsol.help.heat/HeatTransferModuleUsersGuide.pdf, accessed on 11 November 2021.

[81] Avci, E., Mollamahmutoğlu, M.: 'UCS Properties of superfine coment-grounted sand'. Journal of Materials in

Civil Engineering, **28**(12), 2016, 06016015.

[82] Sfarra, S., Ibarra-Castanedo, C., Theodorakeas, P., …, Maldague, X.P.V.: 'Evaluation of the state of conservation of mosaics: simulations and thermographic signal processing', International Journal of Thermal Sciences, **117**, 2017, pp. 287–315.

[83] Yao, Y., Sfarra, S., Lagüela, S., …, Ambrosini, D.: 'Active thermography testing and data analysis for the state of conservation of panel paintings', International Journal of Thermal Sciences, **126**, 2018, pp. 1143–151.

[84] Chrysafi, A.P., Athanasopoulos, N., Siakavellas, N.J.: 'Damage detection on composite materials with active thermography and digital image processing', International Journal of Thermal Sciences, **116**, 2017, pp. 242–253.

[85] Liu, K., Huang, K.-L., Sfarra, S., Yang, J., Liu, Y., Yao, Y.: 'Factor analysis thermography for defect detection of panel paintings', Quantitative InfraRed Thermography Journal, accepted for publication, 2022, DOI: 10.1080/17686733.2021.2019658.